Celestial Mechanics and Dynamical Astronomy (2024) 136:44
https://doi.org/10.1007/s10569-024-10215-1

ORIGINAL ARTICLE

Tidal evolution and spin–orbit dynamics for bodies in the viscous regime

Clodoaldo Ragazzo[1] · **Lucas S. Ruiz**[2]

Received: 31 January 2024 / Revised: 6 September 2024 / Accepted: 9 September 2024 /
Published online: 30 September 2024

Abstract
This study analyzes the secular dynamics of two extended bodies in Keplerian orbits, focusing on tidal effects. It introduces formulas for energy dissipation within each body in a binary system. The bodies can have a finite number of layers with linear viscoelastic rheology. The layers must be sufficiently coupled so that the rotation of each layer remains close to the average rotation of the body. The body is assumed to be in a "viscous regime" (though it may contain purely elastic layers), meaning that the relaxation times of the rheology are much shorter than the typical despinning time and deviations from sphericity are caused only by tidal and centrifugal stresses. The main contribution of this paper is the decomposition of orbital-averaged equations into a fast–slow system. This reduction allows the slow dynamics to be represented as sliding along a torque-free curve with occasional jumps at folding points. This greatly simplifies the analysis of the dynamics as a function of the rheological parameters.

Keywords Tides · Spin-orbit resonance · Secular evolution · Fast-slow system · Viscoelastic rheology

1 Introduction

Newton formulated the law of gravitation and concluded that the motion of the centers of mass of spherical bodies is equivalent to that of point masses. The solution to the resulting two-body problem, as obtained by Newton, forms the backbone of all subsequent developments in celestial mechanics. Notably, while planets and major satellites are almost spherical, even slight deformations caused by spin and tidal forces can significantly influence their rotation and orbits.

Building on the foundational works of Newton, Laplace, Thomson, Darwin, and others, a significant advancement in understanding tidal effects on celestial motion was made by

✉ Lucas S. Ruiz
lucasruiz@unifei.edu.br

Clodoaldo Ragazzo
ragazzo@usp.br

[1] Instituto de Matemática e Estatística, Universidade de São Paulo, São Paulo, SP 05508-090, Brazil

[2] Instituto de Matemática e Computação, Universidade Federal de Itajubá, Itajubá, MG 37500-903, Brazil

Kaula (1964), who decomposed tidal forces harmonically in space and time for two bodies in a Keplerian orbit, using Love numbers to evaluate changes in orbital elements. Recent updates to Kaula's theory are available in Boué and Efroimsky (2019), with additional insights in Efroimsky (2012). Over the last 70 years, extensive research has focused on these tidal effects. Notable contributions include Ferraz-Mello's Ferraz-Mello (2013) model, which builds on Darwin's theory with nonspherical hydrostatic states, detailed further in Folonier et al. (2018), Ferraz-Mello et al. (2020), and summarized in Ferraz-Mello (2019), Ferraz-Mello (2021). Various studies, including those by Goldreich (1966), Singer (1968), Alexander (1973), Mignard (1979), Hut (1981), Makarov and Efroimsky (2013), Correia et al. (2014), Ferraz-Mello (2015), and Boué et al. (2016), have explored deformation equations averaged over orbital motion, particularly in low- and high-viscosity scenarios. The averaged equations used in this work are identical to those presented in Correia and Valente (2022).

In this paper, we study the secular–planar dynamics of two extended bodies. We make the following assumptions:

(1) The two bodies are deformable, nearly spherical at all times;
(2) The spins (or rotation vectors) of the deformable bodies remain perpendicular to the orbital plane.
(3) The bodies are radially stratified, and each body layer is homogeneous and has a linear viscoelastic rheology, see, e.g., Sabadini et al. (2016). Fluid layers, if present, must be sufficiently coupled to the adjacent layers such that the rotation of each layer remains close to the average rotation of the body.
(4) The bodies are assumed to be in a "viscous regime" (though they may contain purely elastic layers), meaning that the relaxation times of the rheology are much shorter than the typical despinning time and deviations from sphericity are caused by tidal and centrifugal stresses.

In this paper, we crucially use that the rheology of a body with a finite number of homogeneous layers is equivalent to that of a homogeneous body with a sufficiently more complex rheology Gevorgyan et al. (2023).

The aim of this study is to analyze the secular dynamics arising from orbital-averaged equations. In the case of a small body orbiting a larger one, where the despin rate of the small body is much higher than that of the larger body, the equations can be further simplified. The main contribution of this work is the decomposition of these simplified equations into a fast–slow system. This reduction allows the slow dynamics to be represented as sliding along a torque-free curve with occasional jumps at folding points. This greatly simplifies the analysis of the dynamics as a function of the rheological parameters.

The equations developed in this paper do not apply to the Sun–Mercury system due to Mercury's permanent deformation. However, this system is used as an example for several reasons:

- Mercury is the only large body in the solar system in a 3:2 spin–orbit resonance. - The averaged equations can be decoupled into fast (spin) and slow (orbital elements) systems, simplifying the dynamical analysis. - Mercury may have been in a viscous regime at the beginning of its history Matsuyama and Nimmo (2009). - Mercury will also serve as a model for a forthcoming paper where we will analyze the transition from a viscous to a solid regime.[1]

[1] By "solid regime," we mean that some relaxation times of the rheology are much longer than the typical despinning time, and the body maintains a permanent (or fossil) deformation, remaining slightly aspherical in the absence of centrifugal and tidal stresses. The intermediate region, where some relaxation times are on the order of the despinning time, will be referred to as the viscous–solid transition regime.

The averaging procedure used in this paper is not suitable for treating a body with permanent deformation (solid regime), as discussed in Sect. 2.12.

In the most widely adopted mechanism for spin–orbit resonance Goldreich and Peale (1966), the probability of Mercury being captured into a particular spin–orbit resonance depends on the permanent deformation of the planetary figure. Larger deformations are needed to make capture likely. Here, Mercury is not assumed to have any permanent deformation. Deformations are the consequences of tides and centrifugal stresses. In our approach, the current 3:2 spin–orbit resonance of Mercury is a transient state that, without any other external influence, can last billions of years until a rapid spin transition occurs, ultimately resulting in Mercury entering a 1:1 spin–orbit resonance state.

In this paper, we show that the probability of the hypothetical viscous Mercury being captured into a 3:2 spin–orbit resonance depends strongly on the rheological parameters. This conclusion, which may be applicable to any binary system and not just the Mercury–Sun system, highlights the importance of employing more complex and realistic rheologies in understanding spin–orbit evolution.

Our findings align with those in Makarov (2012) and Noyelles et al. (2014), where the permanent deformation of Mercury is considered. According to the abstract of Noyelles et al. (2014):

"As opposed to the commonly used constant time lag (CTL) and constant phase lag (CPL) models, the physics-based tidal model changes dramatically the statistics of the possible final spin states."

In this context, the term "physics-based tidal model" refers to a model derived from a rheology with several relaxation times.

We remark that the past capture of Mercury into its current spin–orbit state has been the subject of several previous studies. In our paper, we have completely neglected several important effects that may have been significant, as pointed out in Noyelles et al. (2014): perturbations by other bodies in the Solar System that induce variations in Mercury's eccentricity, the potential relevance of core–mantle–boundary friction at fluid–solid interfaces, the possibility of past impacts with other bodies, existence of a permanent deformation, and changes in the rheology over long timescales. Therefore, our quantitative results regarding the spin–orbit history of Mercury are not intended to describe what actually happened.

In the next section, we present the main results of the paper. The appendices provide several mathematical details involved in deriving these results.

2 Main results

The foundational equations for the orbit and rotation of an extended body are well established in the literature. Various equations detailing the deformation of extended bodies exist. In a companion paper Ragazzo and dos Santos (2024), we averaged the equations provided in Ragazzo and Ruiz (2017) with respect to the orbital motion, excluding the term accounting for the inertia of deformations as discussed in Correia et al. (2018). These equations are applicable to any rheological model. We obtained essentially the same averaged equations as those presented in Correia and Valente (2022). The only difference is the inclusion of a centrifugal deformation term, which is not relevant in the planar case. It is important to emphasize that the averaged equations in Correia and Valente (2022) are more general as they do not necessitate the spins of the bodies to be perpendicular to the orbital plane.

Let m_α and m represent the masses of two celestial bodies, which could be a planet and a star, or a planet and a satellite. We name the bodies such that the "α body" is the largest $m_\alpha \geq m$. The quantities of the large body will always be labeled with an index α and those of the small body will have no label.

We assume that both bodies are almost spherical, deformable, and the deformations are volume preserving. In this situation, the mean moments of inertia, denoted as $\mathrm{I}_\circ$ and $\mathrm{I}_{\circ\alpha}$, remain constant in time, a result attributed to Darwin (Rochester and Smylie 1974).

The motion of the two-body system is determined by three sets of equations: the equations for the relative positions of the centers of mass (orbit), the equations for the rotation of each body about their centers of mass (spin), and the equations for the deformation of each body. In Appendix A, we present these fundamental equations.

2.1 Rheology and Love numbers

The tidal response of a stratified body and the corresponding Love number $k_2(\sigma)$, where σ is the angular frequency of the tidal force, can be determined by solving the mass conservation, momentum conservation, and Poisson equations. Each layer is assumed to be either solid with linear viscoelastic rheology or liquid and inviscid. Viscoelastic layers are modeled with Maxwell rheology, characterized by an elastic shear modulus and viscosity. Liquid layers are treated as viscoelastic layers with a shear modulus approaching zero. As discussed in Sabadini et al. (2016), the Love number can be expressed as a sum of partial fractions, each with a finite number of terms, characterized by an amplitude and a relaxation time.

According to Bland (1960), any linear viscoelastic rheology with a finite number of relaxation times can be represented by a generalized Voigt rheology. The spring–dashpot representation of this is shown in Fig. 1. Specifically, a generalized Voigt model can be constructed with the same relaxation times and amplitudes as those in the Love number of the stratified body.

This generalized Voigt model, along with the association principle in Ragazzo and Ruiz (2017), implies the existence of a hypothetical homogeneous body with the same Love number as the layered body.

This construction is detailed in Gevorgyan et al. (2023), where it is shown that the Love number of either the stratified or the equivalent homogeneous body, after partial fraction expansion, can be written as:

$$k_2(\sigma) = k_\infty + (k_\circ - k_\infty)\left(\frac{h_1}{1+i\tau_1\sigma} + \cdots + \frac{h_{n+1}}{1+i\tau_{n+1}\sigma}\right). \tag{2.1}$$

In these equations:

- The number of relaxation times in the Love number of the stratified body is $n+1$, which is only indirectly related to the number of layers in the body Sabadini et al. (2016). Typically, the number of layers is much smaller than the number of relaxation times.
- $k_\infty := \lim_{\sigma\to\infty} k_2(\sigma)$ is the asymptotic value of the Love number at high frequencies.
- $k_\circ := k_2(0)$ is the Love number at frequency zero, also called secular Love number[2].
- τ_i is the ith characteristic time of the rheology.

[2] The softest possible body is one composed of a perfect fluid, which is held together solely by self-gravity. In this case, $k_\circ = k_f$, where k_f is the fluid Love number. Let R be the body volumetric radius and R_I be the radius of inertia, defined as the radius of a homogeneous sphere of mass m and moment of inertia $\mathrm{I}_\circ$. Assuming that the density is nondecreasing toward the center, the following approximation (valid for$0.2 < \frac{\mathrm{I}_\circ}{mR^2} \leq 0.4$)

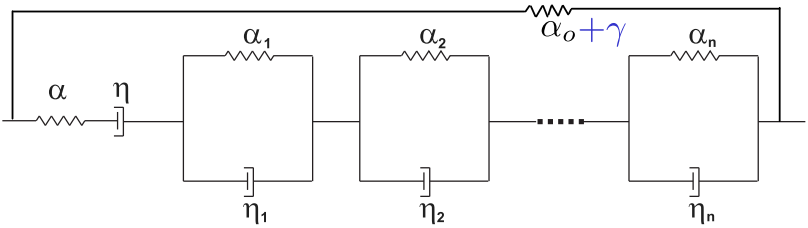

Fig. 1 Generalized Voigt model. The constant γ (blue) represents self-gravity rigidity

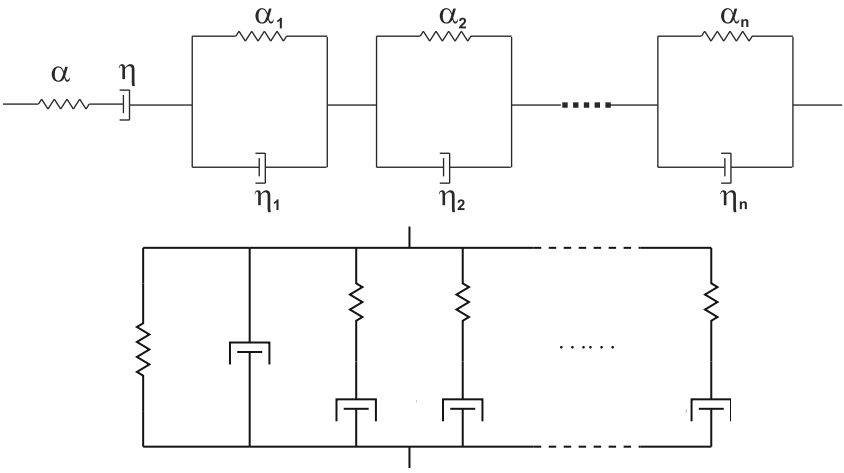

Fig. 2 ABOVE: Generalized Voigt model in Bland (1960) Figure 1.8. BELOW: Generalized Maxwell model Bland (1960) Figure 1.9

- $h_i > 0$ is the relative amplitude of the ith mode of the rheology, which is associated to the characteristic time τ_i. The relative amplitudes add to one:

$$h_1 + h_2 + \cdots h_{n+1} = 1.$$

All the simple rheological models used in the literature, such as Maxwell, Kelvin–Voigt, standard anelastic solid (SAS), Burgers, Bland's generalized Voigt (Fig. 2 above), and Bland's generalized Maxwell (Fig. 2 BELOW), are particular cases of the generalized Voigt rheology depicted in Fig. 1. The Andrade model and the Sundberg–Cooper model can be approximated with arbitrary precision by a generalized Voigt model, as demonstrated in Gevorgyan et al. (2020) and Gevorgyan (2021), respectively.

Footnote 2 continued
holds (Ragazzo 2020, Eqs. 1.2 and 1.8, Theorems 4.1 and 4.2):

$$k_f \approx \frac{3}{2}\left(\frac{R_I}{R}\right)^5 \quad \text{where} \quad R_I^2 := \frac{5}{2}\frac{\mathrm{I}_\circ}{m}\,. \tag{2.2}$$

The maximum value of R_I/R is one, achieved in a homogeneous body, for which $k_f = \frac{3}{2}$. The approximation in equation (2.2) was also proposed in Consorzi et al. (2023).

2.2 Passive deformation

Let $\kappa := \{\mathbf{e}_1, \mathbf{e}_2, \mathbf{e}_3\}$ be an inertial orthonormal frame with origin at the center of mass of the system. The orbit is contained in the plane $\{\mathbf{e}_1, \mathbf{e}_2\}$.

The moment of inertia matrix $\mathbf{I}$ of a body in κ can be written as:

$$\mathbf{I} = \mathrm{I}_\circ(\mathbf{1} - \mathbf{b}), \tag{2.3}$$

where $\mathbf{1}$ is the identity and $\mathbf{b}$ is a symmetric and traceless matrix. We denote matrices and vectors in bold face. The matrix $\mathbf{b}$ is termed the deformation matrix. The deformation matrix of the α-body is denoted as $\mathbf{b}_\alpha$.

Since the bodies are nearly spherical and tidal deformations are minor, the variations in orbital elements occur gradually. As a result, the tidal forces can be approximated by those of point masses undergoing Keplerian motion. Within this framework, tidal forces can be harmonically decomposed both temporally, using Hansen coefficients (see Appendix F), and spatially, using spherical harmonics.

In Appendix B, we employ these decompositions to compute the "passive deformation matrix" in terms of Love numbers, orbital eccentricity, mean motion ($n = \dot{M}$), and the spin angular velocities (ω and ω_α) of each body. The term "passive" refers to the fact that this deformation is computed while neglecting its influence on altering the orbital elements and the spin of each body.

2.3 Frames of reference and the average angular velocity of the principal axes

One of the main issues in the dynamics of deformable bodies is the choice of a "body frame," specifically a moving frame that is either unambiguously defined (the principal axes of inertia) or in which the body is as stationary as possible (the Tisserand mean axis).

A Tisserand frame K has its origin at the center of mass of the body and an angular velocity relative to the inertial frame such that the angular momentum of the body with respect to K is null (see Appendix A). In this paper by the spin of a body, we mean the angular velocity of its Tisserand frame.

Another useful frame is the one determined by the principal axes of inertia, denoted as K_p. This frame describes the average mass distribution of the deformed body and the resulting gravitational field due to deformation. For K_p to be unambiguously defined, the body must always have three distinct axes of inertia, which is always the case in the situation considered in this paper.

For a given passive deformation characterized by (ω, e, n), the orientation of K_p with respect to the inertial frame κ is determined by a single angle ψ of rotation about the $\mathbf{e}_3$ axis. We define the average angular velocity of the principal axes of inertia as:

$$\omega_p(\omega, e, n) := \lim_{t\to\infty} \frac{\psi(t)}{t}. \tag{2.4}$$

In Appendix C, we show that the average angular velocity of the principal axes is always equal to the mean motion n:

$$\omega_p = n. \tag{2.5}$$

This is an expected result if the body is in the viscous regime, as all deformations result from centrifugal and tidal forces, with triaxiality determined by the companion body. As can

be verified in Appendix C, the mathematical derivation of this property from the expression of the passive deformations is not obvious.

Thus, in the viscous regime, the principal axes are always in a one-to-one resonance with the mean motion. The torque, which depends on the geometry and not on the fluid velocity, is very different from the torque in the solid regime. In the solid regime, the principal axes generally move with angular velocities different from the mean motion.

2.4 Energy and angular momentum

The energy function of a system of two rigid spherical bodies is

$$E_\circ := -\frac{Gmm_\alpha}{2a} + \mathrm{I}_\circ \frac{\omega^2}{2} + \mathrm{I}_{\circ\alpha} \frac{\omega_\alpha^2}{2} = -a_1 n^{2/3} + \mathrm{I}_\circ \frac{\omega^2}{2} + \mathrm{I}_{\circ\alpha} \frac{\omega_\alpha^2}{2}, \tag{2.6}$$

where G is the gravitational constant, a is the semi-major axis, and

$$a_1 := \frac{mm_\alpha G^{2/3}}{(m+m_\alpha)^{1/3}}. \tag{2.7}$$

The angular momentum of a spherical body is $\ell_s = \mathrm{I}_\circ \omega$, and the orbital angular momentum is

$$\ell = \frac{mm_\alpha}{m+m_\alpha} a^2 n \sqrt{1-e^2} = a_1 n^{-1/3} \sqrt{1-e^2}. \tag{2.8}$$

The total angular momentum of a system of two spherical bodies is

$$\ell_T := \ell + \ell_s + \ell_{s\alpha}. \tag{2.9}$$

We will assume that $\ell > 0$ (or $n > 0$) and $\ell_T > 0$ for all time.

The energy and angular momentum of a system of two slightly deformable bodies, which are given in Appendix A, are approximately given by the expressions of their spherical approximations.

The total angular momentum is constant, $\dot{\ell}_T = 0$, and within the Lagrangian formalism with dissipation function Ragazzo and Ruiz (2017), the time derivative of the energy is given by the sum of the dissipation functions of each body $\mathcal{D}$ and $\mathcal{D}_\alpha$.

In Appendix D, we use the passive deformations to estimate the average dissipation of energy in each body. For the small body, the result is:

$$\begin{aligned}\langle \mathcal{D} \rangle = -\frac{3}{8} \left(\frac{m_\alpha}{m+m_\alpha} \right)^2 \frac{n^4 R^5}{G} \sum_{k=-\infty}^{\infty} \Bigg\{ \frac{kn}{3} \left(X_k^{-3,0}(e) \right)^2 \mathrm{Im}\, k_2(kn) \\ + (kn - 2\omega) \left(X_k^{-3,2}(e) \right)^2 \mathrm{Im}\, k_2(kn - 2\omega) \Bigg\}.\end{aligned} \tag{2.10}$$

A similar expression holds for the α-body.

In Appendix F, we explain how to evaluate the accuracy of partial sums of this series after truncation in the eccentricity.

Since $\mathrm{Im}\, k_2(-\sigma) = -\mathrm{Im}\, k_2(\sigma)$ and $\mathrm{Im}\, k_2(\sigma) < 0$ for $\sigma > 0$, then $\langle \mathcal{D} \rangle \geq 0$. If $e = 0$, then $X_k^{-3,0}(0) = 0$ for $k \in \mathbb{Z}$ and $X_k^{-3,2}(0) = 0$ for $k \neq 2$. So $\langle \mathcal{D} \rangle = 0$ if and only if $e = 0$ and $n = \omega$.

The energy dissipated due to passive deformations must originate from the motion of the spherical bodies that induce these passive deformations. Consequently, we can infer

$$\begin{aligned}\dot{E}_\circ &= -\frac{2}{3}a_1 n^{-1/3}\dot{n} + \mathrm{I}_\circ \omega\dot{\omega} + \mathrm{I}_{\circ\alpha}\omega_\alpha\dot{\omega}_\alpha \\ &= -2\langle\mathcal{D}\rangle - 2\langle\mathcal{D}_\alpha\rangle.\end{aligned} \tag{2.11}$$

2.5 The average torque and the secular equation for the orbital elements

For the small body, the average torque due to passive deformations is:

$$\langle \mathrm{T}\rangle = -\frac{3}{2}\left(\frac{m_\alpha}{m+m_\alpha}\right)^2 \frac{n^4R^5}{G}\left\{\sum_{k=-\infty}^{\infty}\left(X_k^{-3,2}\right)^2 \mathrm{Im}\, k_2(kn-2\omega)\right\}. \tag{2.12}$$

A similar expression holds for the α-body.

The secular equation for the orbital elements can be readily derived from Eqs. (2.10), (2.11), (2.12), and their counterparts for the α-body:

$$\begin{aligned}\dot{\omega} &= \frac{1}{\mathrm{I}_\circ}\langle \mathrm{T}\rangle, \\ \dot{\omega}_\alpha &= \frac{1}{\mathrm{I}_{\circ\alpha}}\langle \mathrm{T}_\alpha\rangle, \\ \dot{n} &= \frac{3n^{1/3}}{2a_1}\Big(2\langle\mathcal{D}\rangle + 2\langle\mathcal{D}_\alpha\rangle + \omega\langle \mathrm{T}\rangle + \omega_\alpha\langle \mathrm{T}_\alpha\rangle\Big).\end{aligned} \tag{2.13}$$

The conservation of total angular momentum, combined with Eqs. (2.8) and (2.9), implies that the eccentricity, which is featured on the right-hand side of Eq. (2.13), can be expressed in terms of the state variables ω, ω_α, n.

2.6 Timescales and a simplification when $m \ll m_\alpha$

The despin rate is dependent on the imaginary parts of the Love numbers. The largest bodies in the solar system are fluid (e.g., the Sun, Jupiter, etc.) and have an imaginary part of the Love number that is significantly smaller than that of bodies with solid components. Therefore, it is reasonable to assume in the subsequent equations that $\mathrm{Im}\, k_2$ and $\mathrm{Im}\, k_{2\alpha}$ are comparable or $\mathrm{Im}\, k_2 \gg \mathrm{Im}\, k_{2\alpha}$.

The ratio between the despin rates, assuming no spin–orbit resonances, is given by

$$\frac{\dot{\omega}}{\dot{\omega}_\alpha} \approx \frac{\mathrm{I}_{\circ\alpha}}{\mathrm{I}_\circ}\frac{m_\alpha^2}{m^2}\frac{R^5}{R_\alpha^5}\frac{\mathrm{Im}\, k_2}{\mathrm{Im}\, k_{2\alpha}} \approx \frac{\rho_\alpha}{\rho}\frac{m_\alpha^2}{m^2}\frac{\mathrm{Im}\, k_2}{\mathrm{Im}\, k_{2\alpha}}, \tag{2.14}$$

where ρ represents the density of the body. If $m_\alpha \gg m$, then $\dot{\omega} \gg \dot{\omega}_\alpha$, indicating that the despin rate of the larger body is significantly slower than that of the smaller body. In such a case, as a first approximation, we may assume ω_α =constant and Eq. (2.13) becomes:

$$\begin{aligned}\dot{\omega} &= \frac{1}{\mathrm{I}_\circ}\langle \mathrm{T}\rangle, \\ \dot{n} &= \frac{3n^{1/3}}{2a_1}\Big(2\langle\mathcal{D}\rangle + 2\langle\mathcal{D}_\alpha\rangle + \omega\langle \mathrm{T}\rangle\Big).\end{aligned} \tag{2.15}$$

For example, for the Sun–Mercury system, using $-\mathrm{Im}\, k_{2\alpha} \approx 3.5 \times 10^{-8}$ Ogilvie (2014) and $-\mathrm{Im}\, k_2 \approx 0.011$ (Baland et al. 2017, p. 152), we obtain $\frac{\dot{\omega}}{\dot{\omega}_\alpha} \approx 6 \times 10^{17}$.

2.7 A simplification when the α body is fluid (almost inviscid)

The ratio of the energy dissipation rates in each body is given by

$$\frac{\langle \mathcal{D} \rangle}{\langle \mathcal{D}_\alpha \rangle} \approx \frac{m_\alpha^2}{m^2} \frac{R^5}{R_\alpha^5} \frac{\mathrm{Im}\, k_2}{\mathrm{Im}\, k_{2\alpha}} \approx \frac{\rho_\alpha^2}{\rho^2} \frac{R_\alpha}{R} \frac{\mathrm{Im}\, k_2}{\mathrm{Im}\, k_{2\alpha}}. \tag{2.16}$$

Equation (2.16), along with the equation for $\dot{n}$ in (2.15), implies that depending on the imaginary parts of the Love numbers, the larger body may play a more significant role than the smaller body in altering the orbital elements[3].

However, when the α body consists of a low-viscosity fluid and the smaller body includes a solid part, then $\frac{\mathrm{Im}\, k_2}{\mathrm{Im}\, k_{2\alpha}} \gg 1$, and $\frac{\langle \mathcal{D} \rangle}{\langle \mathcal{D}_\alpha \rangle}$ may also be significantly greater than one. This scenario applies to the Sun–Mercury system, where $\frac{\langle \mathcal{D} \rangle}{\langle \mathcal{D}_\alpha \rangle} \approx 2.8 \times 10^6$. In such cases, $\langle \mathcal{D}_\alpha \rangle$ can be neglected in comparison to $\langle \mathcal{D} \rangle$ in the equation for $\dot{n}$ in (2.15).

Therefore, for the Sun–Mercury system, we can employ the following approximation to Eq. (2.13):

$$\begin{aligned} \dot{\omega} &= \frac{1}{\mathrm{I}_\circ} \langle \mathrm{T} \rangle, \\ \dot{n} &= \frac{3n^{1/3}}{2a_1} \Big(2\langle \mathcal{D} \rangle + \omega \langle \mathrm{T} \rangle \Big), \end{aligned} \tag{2.18}$$

where the state variables are (ω, n). This type of equation commonly appears in the literature, as seen in references such as Correia et al. (2014), Gomes et al. (2019), and Correia and Valente (2022).

The angular momentum, which remains constant along the motion, becomes simpler:

$$\ell_T = a_1 n^{-1/3} \sqrt{1 - e^2} + \mathrm{I}_\circ \omega. \tag{2.19}$$

Equations (2.18) are equivalent to those obtained in Correia and Valente (2022) in the planar case.

2.8 The slow–fast dynamics when $\frac{\mathrm{I}_\circ}{ma^2} \ll 1$

In the remainder of this section, we consider the simplest case where Eq. (2.18) is applicable, with $m \ll m_\alpha$ and $|\mathrm{Im}\, k_{2\alpha}| \ll |\mathrm{Im}\, k_2|$.

[3] For the Earth–Moon system, using the Love number $k_{2\alpha} = 0.2817 - 0.02324\, i$ for the Earth (Ragazzo and Ruiz 2017, Table 3, semidiurnal frequency), and $\mathrm{Im}\, k_2$ =-5.13 $\times 10^{-4}$ for the Moon (orbital frequency) Fienga et al. (2019), we obtain

$$\frac{\langle \mathcal{D} \rangle}{\langle \mathcal{D}_\alpha \rangle} \approx \frac{m_\alpha^2 R^5}{m^2 R_\alpha^5} \frac{\mathrm{Im}\, k_2}{\mathrm{Im}\, k_{2\alpha}} = 0.022. \tag{2.17}$$

This indicates that the Earth's influence on altering the orbital parameters is greater than that of the Moon.

The ratio

$$\frac{\dot{n}}{\dot{\omega}} = \frac{\mathrm{I}_\circ n^{4/3}}{a_1}\frac{3\omega}{2n}\left\{1 + \frac{\dfrac{1}{2\omega}\left\{\displaystyle\sum_{k=-\infty}^{\infty}\frac{kn}{3}\left(X_k^{-3,0}(e)\right)^2 \operatorname{Im} k_2(kn) + \cdots\right\}}{\displaystyle\sum_{k=-\infty}^{\infty}\left(X_k^{-3,2}\right)^2 \operatorname{Im} k_2(kn-2\omega)}\right\} \tag{2.20}$$

includes the factor

$$\frac{\mathrm{I}_\circ n^{4/3}}{a_1} = \frac{1}{m}\left(1+\frac{m}{m_\alpha}\right)\frac{\mathrm{I}_\circ}{a^2} \approx \frac{\mathrm{I}_\circ}{ma^2}. \tag{2.21}$$

We assume

$$\frac{\mathrm{I}_\circ n^{4/3}}{a_1} \approx \frac{\mathrm{I}_\circ}{ma^2} \ll 1. \tag{2.22}$$

For the Sun–Mercury system,

$$\frac{\mathrm{I}_\circ n^{4/3}}{a_1} = 6.2\times 10^{-10}. \tag{2.23}$$

In this case, if $\left|\frac{\omega}{n}\right|$ is not far from one and (n,ω) is not on

$$\mathcal{C} := \left\{(n,\omega) : \sum_{k=-\infty}^{\infty}\left(X_k^{-3,2}(e)\right)^2 \operatorname{Im} k_2(kn-2\omega) = 0\right\} \quad \text{(torque-free curve)}, \tag{2.24}$$

then $\frac{\dot{\omega}}{\dot{n}} \gg 1$. As a result, the spin–orbit dynamics is governed by a slow–fast system of equations, where n is the slow variable and ω is the fast variable. The typical dynamics is described in the caption of Fig. 3.

Due to inequality (2.22), Eq. (2.19) can be simplified to

$$\frac{\ell_T}{n\,\mathrm{I}_\circ} = \frac{a_1}{\mathrm{I}_\circ n^{4/3}}\sqrt{1-e^2} + \frac{\omega}{n} \approx \frac{a_1}{\mathrm{I}_\circ n^{4/3}}\sqrt{1-e^2}, \tag{2.25}$$

where we have used that $\left|\frac{\omega}{n}\right|$ is not far from one and e is not close to one. This leads to the approximation

$$e \approx \sqrt{1-\left(\frac{\ell_T^3}{a_1^3}n\right)^{2/3}}. \tag{2.26}$$

The constant $\frac{\ell_T^3}{a_1^3}$ has the unit of time. (For the Sun–Mercury system, $\frac{\ell_T^3}{a_1^3} = 13.1224$ days[4].) We use this constant to define the nondimensional mean motion ν and spin angular velocity w, which are used in Fig. 3:

$$\nu := \frac{\ell_T^3}{a_1^3}n \qquad \mathrm{w} := \frac{\ell_T^3}{a_1^3}\omega. \tag{2.27}$$

[4] $2\pi\frac{\ell_T^3}{a_1^3} = 82.45$ days is approximately the period of the longest possible synchronous, $\omega = n$, circular orbit of Mercury about the Sun.

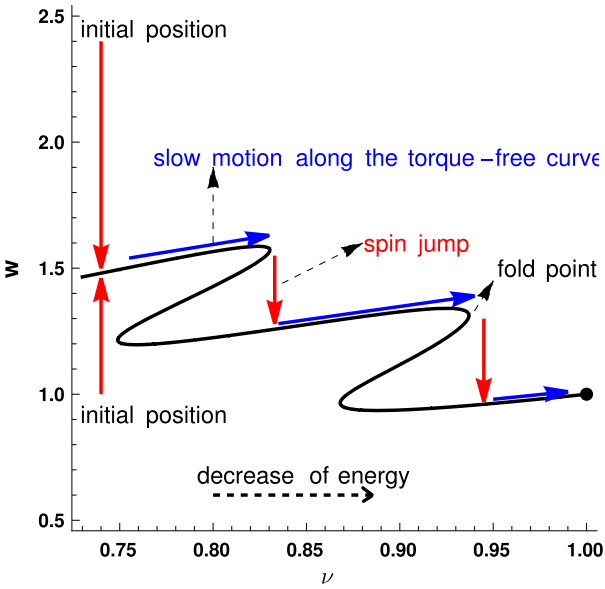

Fig. 3 Typical dynamics when $\frac{ma^2}{I_\circ} \gg 1$. We use the nondimensional mean motion $\nu = \frac{\ell_T^3}{a_1^3} n$ and the nondimensional spin angular velocity $\mathrm{w} = \frac{\ell_T^3}{a_1^3} \omega$ in the plot, as seen in Eq. (2.27) and the previous paragraphs. The curve in black represents the torque-free curve $\mathcal{C}$: $\dot{\mathrm{w}} < 0$ above $\mathcal{C}$, $\dot{\mathrm{w}} > 0$ below $\mathcal{C}$, and $\dot{\mathrm{w}} = 0$ on $\mathcal{C}$. A solution whose initial condition is above $\mathcal{C}$ converges rapidly to $\mathcal{C}$ with a decreasing spin velocity, while a solution whose initial condition is below $\mathcal{C}$ converges rapidly to $\mathcal{C}$ with an increasing spin velocity. Upon reaching $\mathcal{C}$, the solution gradually progresses along $\mathcal{C}$. The decrease in energy implies that ν increases along $\mathcal{C}$ (with e decreasing). The motion along $\mathcal{C}$ is sustainable up to a fold point. At this point, the decrease in energy forces the solution to depart from $\mathcal{C}$, resulting in a spin jump. The solution is then drawn toward another point on $\mathcal{C}$, representing a lower-order spin–orbit resonance. Eventually, the solution approaches the synchronous solution $(\nu, \mathrm{w}) \approx (1, 1)$. For a general discussion on the flow close to $\mathcal{C}$, see Ragazzo and dos Santos (2024)

2.9 Mercury's Love number

Mercury is not in hydrostatic equilibrium: The expected hydrostatic flattening is two orders of magnitude lower than the observed flattening. Therefore, the theory in this paper for bodies in the viscous regime is not valid for the current state of Mercury[5].

Our goal in the following sections is to demonstrate how variations in the rheological parameters impact the capture by spin–orbit resonances, rather than to explain Mercury's actual history. To simplify our analysis, we will use the current Love number of Mercury at its orbital frequency to constrain the rheological parameters.

For Mercury, at the orbital frequency

$$n_{\mathrm{mer}} = \frac{2\pi}{87.969 \text{ days}}, \tag{2.28}$$

[5] However, for its first 0.2 Gyr, Mercury was presumed hot and in the viscous regime (see Matsuyama and Nimmo (2009) paragraph [61]). According to Breuer et al. (2007), the lithospheric thickness reached roughly 150 km at the end of this period. This suggests the presence of secular elastic rigidity, represented by $\alpha_0 > 0$ in Fig. 1, in conjunction with self-gravity, such that $k_\circ < k_f$, where k_f denotes the fluid Love number.

current estimates of the Love number fall within the range $0.53 < \mathrm{Re}\, k_2 < 0.63$, with the preferred value being $k_2 = 0.569$ Genova et al. (2019), Goossens et al. (2022), and $0 < -\mathrm{Im}\, k_2 < 0.025$ (Baland et al. 2017, p. 152) (Steinbrügge et al. 2018, p.2767 and 2769). We will assume

$$k_R := \mathrm{Re}\, k_2 = 0.57 \quad \text{and} \quad k_I := \mathrm{Im}\, k_2 = -0.011 \tag{2.29}$$

as reference values (quality factor $Q \approx -\frac{\mathrm{Re}\, k_2}{\mathrm{Im}\, k_2} \approx 52$).

We will consider $k_\circ$ as a free parameter. It can vary either as a consequence of changes in the mean moment of inertia $\mathrm{I}_\circ$ (according to Eq. (2.2)) or due to the presence of a purely elastic layer. In the absence of inertia of deformation, the real part of the Love number decreases with the frequency Correia et al. (2018). Equation (2.2) implies that $k_f = 1.04$, and therefore,

$$0.57 = k_R < k_\circ \leq k_f = 1.04. \tag{2.30}$$

2.10 Mercury with one relaxation time

The generalized Voigt model with a single relaxation time is represented by a spring–dashpot model shown in Fig. 1 with $n = 0$. This is the rheology of the commonly called standard linear solid. The Love number is described by Eq. (2.1) with $n = 0$:

$$k_2(\sigma) = k_\infty + (k_\circ - k_\infty).\frac{1}{1 + i\tau\sigma}. \tag{2.31}$$

We impose $k_2(n_{\mathrm{mer}}) = 0.57 - 0.011i$ and find that only one parameter among the three $k_\infty, k_\circ$, and τ can vary freely.

We will first illustrate the enlargement of the basin of attraction of Mercury's current state under the variation of the parameter $k_\circ$. By "basin of attraction," we mean the entire set of past states that are mapped into a small region centered at Mercury's current state. Since the timescale for significant motion along the torque-free curve is on the order of billions of years and Mercury has existed for at most 5 billion years, all past states beyond 5 billion years that are in the basin of attraction of Mercury's current state are not physically realizable.

In Fig. 4 LEFT panel, we show the torque-free curve for $k_\circ = 0.8$. The current state of Mercury is covered by part of the torque-free curve close to the resonance line $\frac{\omega}{n} = 2$. This implies that Mercury must have been captured directly into the 3:2 spin–orbit resonance, without prior transitions through higher-order resonances.

In Fig. 4 RIGHT panel, we show the torque-free curve for $k_\circ = 0.7$, which implies $k_\infty = 0.5691$ and $\tau n_{\mathrm{mer}} = 11.89$. In this scenario, the current state of Mercury suggests that it could have been captured in a higher-order resonance before settling into the 3:2 spin–orbit resonance. The potential initial states of Mercury that lead to its current state, as indicated by the region hatched with vertical lines in the RIGHT panel, encompass a much larger set than the corresponding region in the LEFT panel.

We will say that the state of Mercury is *covered* by the resonance $\frac{\omega}{n} = 2$ when the situation in Fig. 4 LEFT holds and not covered when the situation in Fig. 4 RIGHT holds. If Mercury's current state is covered by the resonance $\frac{\omega}{n} = 2$, then its basin of attraction is small otherwise it is large, as show by the hatched regions in Fig. 4.

The phenomenon of the enlargement of the basin of attraction of Mercury's current state occurs in the same way as in the case of two relaxation times.

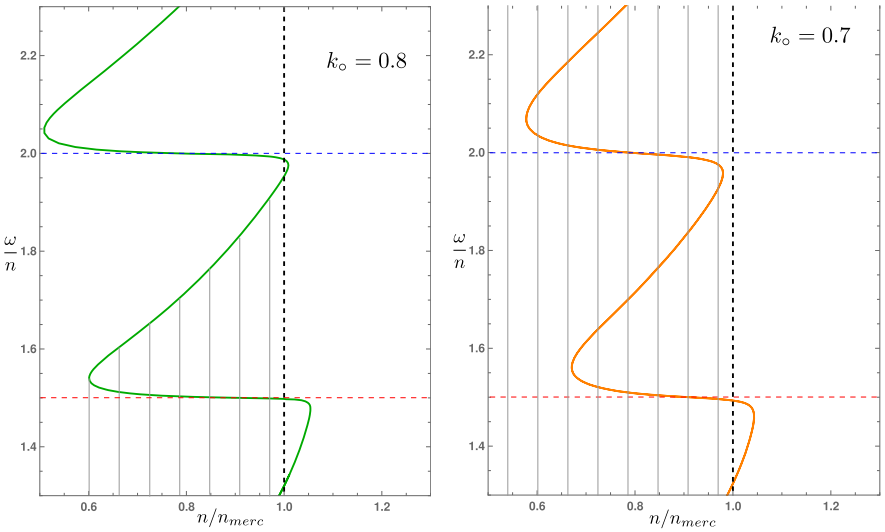

Fig. 4 LEFT: Torque-free curve (green) for Mercury with $k_\circ = 0.8$, $k_\infty = 0.5695$, and one relaxation time: $\tau n_{\text{merc}} = 20.91$. Two spin–orbit resonance lines (horizontal dashed) are shown. Mercury is currently on the $3n = 2\omega$ resonance line, and its mean motion is normalized to one, represented by the vertical dashed line. The region hatched with vertical black lines represents potential initial positions of Mercury that could have led to its current state. In this case, we say that the resonance $\frac{\omega}{n} = 2$ covers Mercury's state. RIGHT: Torque-free curve (orange) for Mercury with $k_\circ = 0.7$ and one relaxation time: $\tau n_{\text{mer}} = 11.82$. The remainder of the notation is the same as that in the left panel. In this case, we say that the resonance $\frac{\omega}{n} = 2$ does not cover Mercury's state

The effect of varying $k_\circ$ on the shape of the torque-free curve is shown in Fig. 5. Given that $k_2(n_{\text{mer}}) = 0.57 - 0.011i$, we have:

$$\tau n_{\text{mer}} = \frac{k_\circ - k_R}{-k_I} = \frac{k_\circ - 0.57}{0.011} \tag{2.32}$$

and

$$k_\infty = \frac{-0.011 + 0.57\tau n_{\text{mer}}}{\tau n_{\text{mer}}}. \tag{2.33}$$

2.11 Mercury with two relaxation times

The generalized Voigt model with two relaxation times is represented by a spring–dashpot model shown in Fig. 1 with $n = 1$. This rheology is commonly called Burgers rheology.

In this case, Eq. (2.1) implies

$$k_R + k_I\, i = k_\infty + (k_\circ - k_\infty)\left(\frac{h_1}{1 + i\tau_1 n_{\text{mer}}} + \frac{h_2}{1 + i\tau_2 n_{\text{mer}}}\right), \tag{2.34}$$

where $k_R = 0.57$, $k_I = -0.011$, $\tau_1 < \tau_2$, and $h_2 = 1 - h_1$.

We will consider $k_\circ$, τ_1, and τ_2 as free parameters.

As shown in Appendix E, the requirement $0 < h_1 < 1$ implies

$$\tau_1 < \tau_c < \tau_2, \tag{2.35}$$

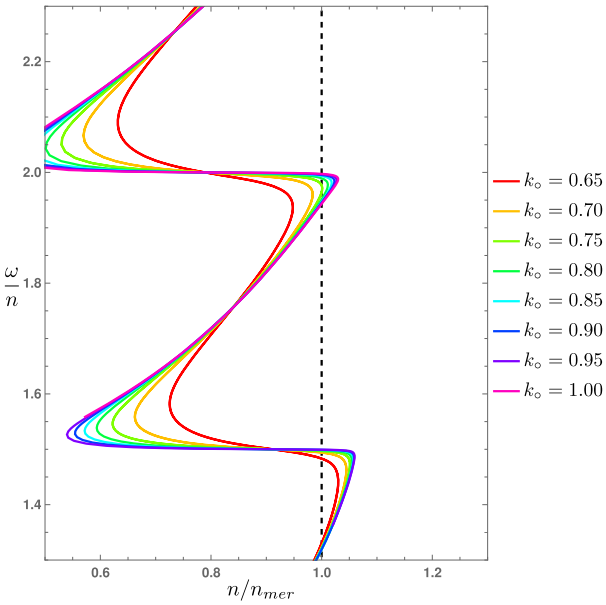

Fig. 5 Torque-free curves for the rheology with a single relaxation time τ (standard linear solid). The dependence of τ on $k_\circ$ is given in Eq. (2.32). The value $k_\circ = 0.746$ is critical for the enlargement of the basin of attraction of Mercury's current state. For $k_\circ > 0.746$, the basin of attraction is small, and for $k_\circ < 0.746$, it is large, as shown in Fig. 4 and discussed in the text

where

$$n_{\text{mer}}\tau_c := \frac{k_\circ - k_R}{-k_I} = \frac{k_\circ - 0.57}{0.011} \tag{2.36}$$

is the value of τ in the single-relaxation-time case for given $(k_R, k_I, k_\circ)$, as shown in Eq. (2.32). Moreover, if τ_2 is fixed, then

$$\lim_{\tau_1 \to \tau_c} h_1(\tau_1, \tau_2) = 1 \Rightarrow h_2 \to 0, \tag{2.37}$$

returning us to the single-relaxation-time situation.

In Figs. 6 and 7, we show the torque-free curve for $n_{\text{mer}}\tau_2 = 2011.6$, several values of $n_{\text{mer}}\tau_1 < n_{\text{mer}}\tau_c$, and $k_\circ = 0.9$ and $k_\circ = 0.7$, respectively. The most distinct feature of the torque-free curve in this case, compared to the single-relaxation-time case, is the appearance of an extra fold close to the resonance lines, as detailed in the RIGHT panel of Fig. 6. This extra fold disappears as $\tau_1 \to \tau_c$, and in this limit, the torque-free curve of the two-relaxation-time rheology becomes the torque-free curve of the single-relaxation-time case.

Another difference between the one-relaxation-time and the two-relaxation-time cases is that the range of values of $k_\circ$ for which the current state of Mercury is not covered by the resonance $\frac{\omega}{n} = 2$ is larger in the latter. For instance, in Fig. 6, there is a set of values of τ_1 for which the state of Mercury is not covered, indicating a large basin of attraction, and the remaining values of τ_1 such that the state of Mercury is covered, with a respective small basin. The upper tongue of the torque-free curves covers Mercury's state for smaller values of τ_1 while the lower tongue covers it for larger values of τ_1.

Figure 8 illustrates the sensitivity of the basin of attraction of Mercury's current state to variations in $k_\circ$. For $k_\circ = 0.8$ and $k_\circ = 0.9$, we present the parameter values in the (τ_1, τ_2) space where the current state of Mercury is either covered (small basin of attraction of the current state of Mercury) or not covered by the resonance $\frac{\omega}{n} = \frac{4}{2}$ (large basin of attraction of the current state of Mercury). The regions where the current state is covered are

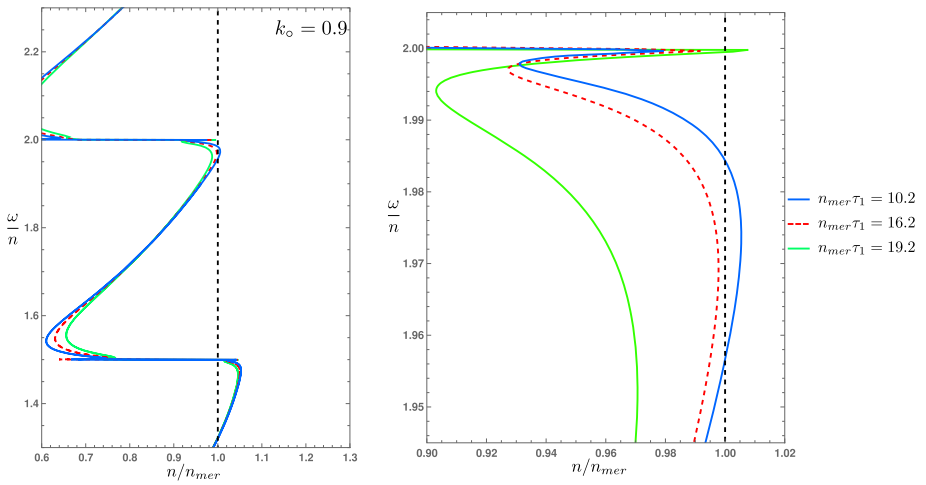

Fig. 6 Torque-free curves for the rheology (Burgers) with two relaxation times for $k_\circ = 0.9$, $n_{\rm mer}\tau_2 = 2011.6$, and some values of $n_{\rm mer}\tau_1 < n_{\rm mer}\tau_c = 20.9$. The right panel shows the details close to the resonance $\frac{\omega}{n} = 2$

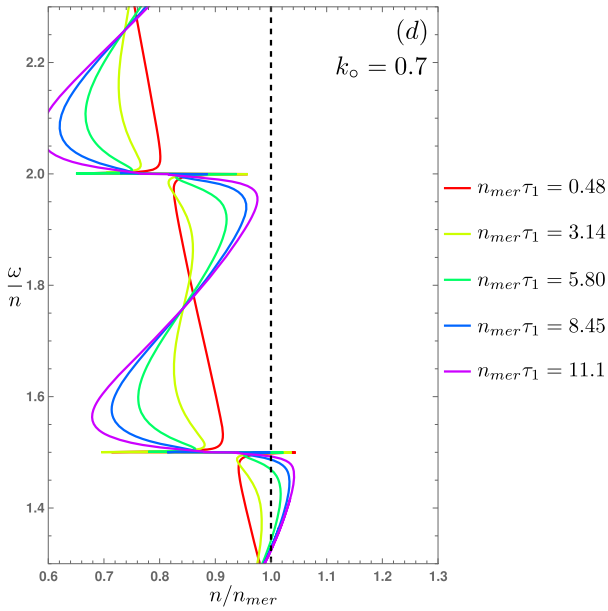

Fig. 7 Torque-free curves for the rheology (Burgers) with two relaxation times for $k_\circ = 0.7$, $n_{\rm mer}\tau_2 = 2011.6$, and several values of $n_{\rm mer}\tau_1 < n_{\rm mer}\tau_c = 11.8$

indicated in red, and the regions where it is not covered are indicated in blue. In both cases, for a sufficiently large fixed value of τ_2, there are two red intervals of τ_1. Different parts of the torque-free curve cover the current state of Mercury in each one of these intervals, as illustrated by the three curves in Fig. 6.

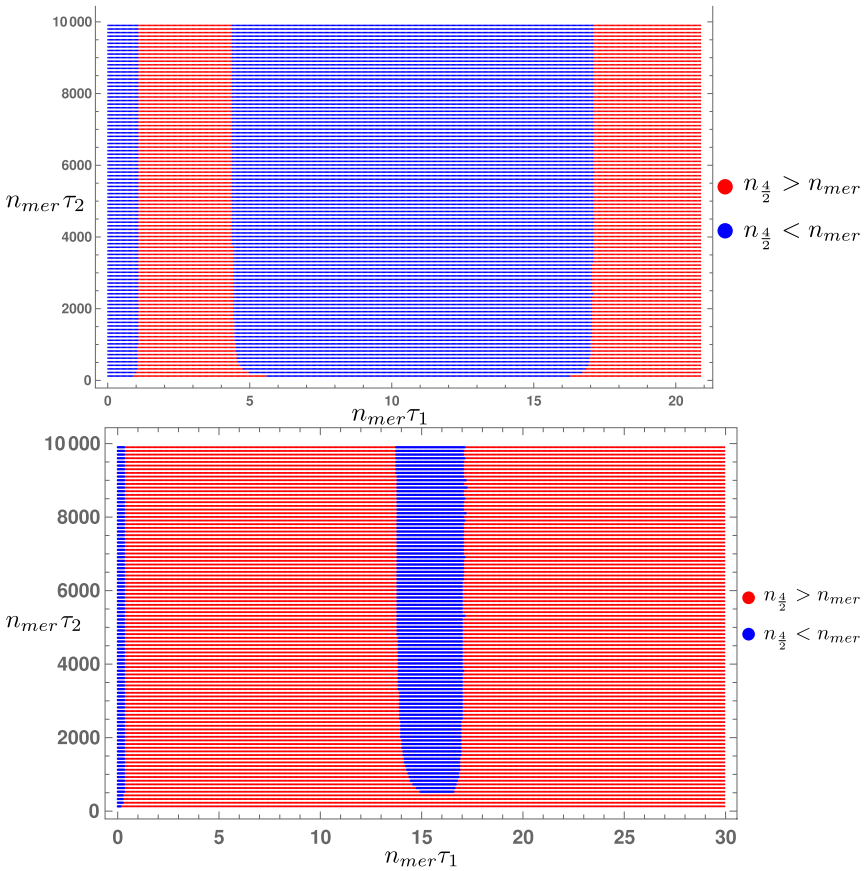

Fig. 8 Regions in the (τ_1, τ_2) space where the current state of Mercury is covered (red) or not (blue) by the resonance $\frac{\omega}{n} = \frac{4}{2}$. In the ABOVE panel, $k_\circ = 0.8$, and in the BELOW panel, $k_\circ = 0.9$

Table 1 Exact values of ω/n_{mer} for which the average torque in Fig. 5 is zero at $n = n_{\text{mer}}$

$k_\circ$	0.65	0.7	0.75	0.8	0.85	0.9	0.95	1.0
τn_{mer}	7.3	11.8	16.4	20.9	25.5	30.0	34.5	39.1
ω/n_{mer}	1.4835	1.4941	1.4969	1.4981	1.4987	1.4991	1.4993	1.4995

2.12 One very large relaxation time: consequences and breakdown of the averaging procedure

The spin state of the hypothetical Mercury considered in this paper, after a relatively fast transient, settles on the torque-free curve. As shown in Fig. 5 and more precisely in Table 1, for a rheology with a single relaxation time, the values of ω/n_{mer} for the hypothetical Mercury are always below $\omega/n = 3/2$. However, as τ increases, ω/n_{mer} approaches $3/2$.

The same phenomenon occurs for a rheology with two relaxation times. If we fix all rheological parameters except τ_2, the value of ω/n_{mer} on the torque-free curve gets closer to

3/2 as τ_2 increases. For example, for a rheology with two relaxation times, with $k_\circ = 0.9$, $n_{\rm mer}\tau_1 = 0.03$, $\tau_2 = \tau_1 \times 10^6$, and the other parameters determined as in Sect. 2.11, the average torque is zero at $\omega/n_{\rm mer} = 1.5 - 8.7 \times 10^{-7}$, which is very close to, but still below, the observed value.

The reason for the torque-free value of $\omega/n_{\rm mer}$ being always below the 3/2 was explained to us by M. Efroimsky: "the root of the torque-free curve (in Fig. 9a, b) is slightly displaced from $\frac{\omega}{n_{\rm mer}} = \frac{3}{2}$ to the left because the kink is superimposed with a vertical bias coming from the tail of the diurnal kink." This is clearly shown in Fig. 9c, which is a blow-up of Fig. 9b at $\frac{\omega}{n_{\rm mer}} = \frac{3}{2}$[6].

The dashed black curve, $T_{\frac{3}{2}}$, in Fig. 9 (c) is the graph of the kink associated with the resonance $\frac{\omega}{n_{\rm mer}} = \frac{3}{2}$, which corresponds to the term $k = 3$ in the average torque in Eq. (2.12):

$$T_{\frac{3}{2}} = -\frac{3}{2}\left(\frac{m_\alpha}{m+m_\alpha}\right)^2 \frac{n^4 R^5}{G}\left\{\left(X_3^{-3,2}\right)^2 \mathrm{Im}\, k_2(3n-2\omega)\right\}. \tag{2.38}$$

The "diurnal kink" is the term corresponding to $k = 2$:

$$T_1 = -\frac{3}{2}\left(\frac{m_\alpha}{m+m_\alpha}\right)^2 \frac{n^4 R^5}{G}\left\{\left(X_2^{-3,2}\right)^2 \mathrm{Im}\, k_2(2n-2\omega)\right\}. \tag{2.39}$$

The tail of the diurnal kink at $\frac{\omega}{n_{\rm mer}} = \frac{3}{2}$ is negative and displaces the kink associated with $k = 3$, as shown by the dashed red curve in Fig. 9c.

Figure 7 clearly shows that for large values of $\tau_2 n_{\rm mer}$, the torque-free curve becomes almost constant at the values 3/2 and 2, and this also occurs for other half-integers. Bodies with permanent deformations, like the actual Mercury, have spin–orbit resonances exactly at half-integers. This suggests that for very large $\tau_2 n_{\rm mer}$, the rheological behavior of bodies in the viscous regime becomes closer to that of bodies in the solid regime. Although this claim is correct and was used in Ragazzo et al. (2022) to define the "prestress frame," the averaging method applied in this paper cannot be used in this situation.

The reason for the breakdown of the averaging procedure is as follows. The averaging method relies on the fact that the typical variation rate of the spin ω and orbital elements (e, n) is small compared to the typical variation rate of the deformation variables. This allows for the computation of the deformation for frozen values of (ω, e, n) (the passive deformations). These passive deformations are then used to average the equations for (ω, e, n). However, when one of the relaxation times is not much smaller than the characteristic despinning time, the perturbative scheme used in this paper breaks down.

For Mercury, an estimate of the despin time, defined as (Noyelles et al. 2014, Eq. 20)

$$\tau_{\rm despin} = \frac{|\omega|}{|\dot{\omega}|} = \left|\frac{\omega\, \mathrm{I}_\circ}{\langle T\rangle}\right|,$$

can be obtained using Eq. (2.12). The result is of the same order as that reported in (Noyelles et al. 2014, Section 5), approximately 10 Myr. The value of $\tau_2 n_{\rm mer} = 0.03 \times 10^6 n_{\rm mer} = 1150$ yr used above to obtain the torque-free value $\omega/n_{\rm mer} = 1.5 - 8.7 \times 10^{-7}$ is approximately $10^{-4}\tau_{despin}$ for Mercury.

There are two pieces of evidence indicating the unsuitability of the averaging method used in this paper when $\tau_2 n_{\rm mer}$ is large. First, although $\omega/n_{\rm mer} \approx 3/2$ for arbitrarily large $\tau_2 n_{\rm mer}$,

[6] Our Fig. 9 is essentially the same as Figure 5 in Makarov et al. (2012) and Figure 3 in Makarov and Efroimsky (2013)

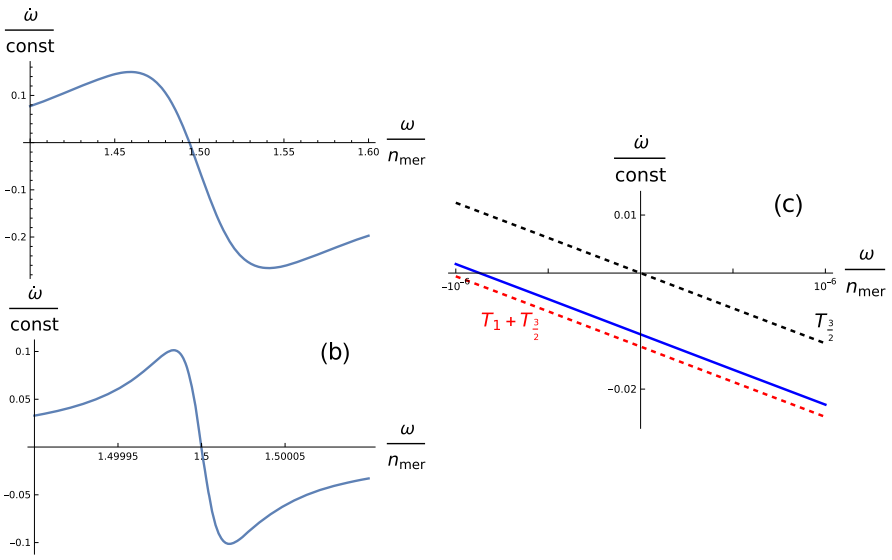

Fig. 9 Three graphs of $\dot{\omega} = \frac{\langle T \rangle}{\mathrm{I}_\circ}$ divided by the constant $(k_\circ - k_\infty)\frac{3n_{\mathrm{mer}}^4 R^5}{2G\,\mathrm{I}_\circ}$ are presented as a function of $\frac{\omega}{n_{\mathrm{mer}}}$ for $n = n_{\mathrm{mer}}$ fixed. **a** Rheology has a single relaxation time: $n_{\mathrm{mer}}\tau = 11.89$, $k_\circ = 0.7$, and $k_\infty = 0.5691$. $\dot{\omega} = 0$ for $\omega/n_{\mathrm{mer}} = 1.49413$. **b** Rheology with two relaxation times: $n_{\mathrm{mer}}\tau_1 = 0.03$, $n_{\mathrm{mer}}\tau_2 0.03 \times 10^6$, $h_1 = 0.52654$, $k_\circ = 0.9$, and $k_\infty = 0.2033$. $\dot{\omega} = 0$ for $\omega/n_{\mathrm{mer}} = 1.5 - 8.7 \times 10^{-7}$. **c** is detail of **b** where the full blue curve is the graph of the complete torque, including all terms, and the black dashed $\left(T_{\frac{3}{2}}\right)$ and red dashed $\left(T_{\frac{3}{2}} + T_1\right)$ curves are two approximations, see text for explanations. The curve $T_{\frac{3}{2}}$ has a zero exactly at $\frac{\omega}{n_{\mathrm{mer}}} = 1.5$

the principal axes of inertia still have an average angular speed of $\omega_p = n$ (see Sect. 2.3). This is clearly in contradiction with what is expected in the solid regime, as in Mercury, where the spin–orbit resonance is between the rotation rate of the principal axes of inertia and the mean motion.[7]

A second piece of evidence comes from Fig. 7, where we observe a pinch in the torque-free curve along the values $\omega/n = 3/2$ and $\omega/n = 2$. The space between the upper and lower branches of the torque-free curve at $\omega/n = 3/2$ is so small that a minor perturbation can move the state from above the upper branch to below the lower branch, causing it to move toward the resonance at $\omega/n = 1$. As τ_2 increases, this pinch becomes more pronounced.

2.13 Conclusion

In this paper, we have derived equations for the secular evolution of spin and orbit due to tidal effects using energy arguments. The body is assumed to be in a viscous regime, where the lack of sphericity is only due to centrifugal and tidal forces, and the body does not have any permanent deformation. The body's rheology can be quite general. The equations were originally obtained by other authors, notably in Correia and Valente (2022).

[7] Note: Mercury likely has a liquid core. Is it possible that the fluid in the core has a slightly different average velocity from that of the mantle? In this case, the average velocity of the Tisserand frame could be slightly displaced from the exact resonance value of 3/2. However, the principal axes of inertia would still be in perfect 3:2 resonance.

In many cases, such as for Mercury, which served as a model in our study, the equations can be further simplified. A major contribution of this paper is the decomposition of these simplified equations into a fast–slow system. This reduction allows the slow dynamics to be represented as sliding along the torque-free curve with occasional jumps at folding points. This greatly simplifies the analysis of the dynamics as a function of the rheological parameters.

Finally, we emphasize that the averaged equations obtained in this paper fail when one of the relaxation times is not much smaller than the typical despin time. As one of the relaxation times tends to infinity, the body transitions from a viscous regime to a solid regime, where permanent deformation is likely to appear. The analysis of this limit will be addressed in a forthcoming paper.

A The fundamental equations

Let $\mathbf{x}$ be the vector in the inertial frame κ from the center of mass of the small body to the body α. The equation for the orbital motion is

$$\begin{aligned}\ddot{\mathbf{x}} = G(m_\alpha + m)\Bigg\{ &- \frac{\mathbf{x}}{|\mathbf{x}|^3} - \frac{15}{2}\frac{1}{|x|^7}\left(\left(\frac{\mathrm{I}_{\circ\alpha}}{m_\alpha}\mathbf{b}_\alpha + \frac{\mathrm{I}_\circ}{m}\mathbf{b}\right)\mathbf{x}\cdot\mathbf{x}\right)\mathbf{x} \\ &+ 3\frac{1}{|\mathbf{x}|^5}\left(\frac{\mathrm{I}_{\circ\alpha}}{m_\alpha}\mathbf{b}_\alpha + \frac{\mathrm{I}_\circ}{m}\mathbf{b}\right)\mathbf{x}\Bigg\},\end{aligned} \tag{A.40}$$

where the deformation matrix of the small body $\mathbf{b}$, defined in Eq. (2.3), is given by

$$\mathbf{b} = \begin{pmatrix} b_{11} & b_{12} & 0 \\ b_{12} & b_{22} & 0 \\ 0 & 0 & b_{33} \end{pmatrix}, \quad \text{with} \quad b_{33} = -b_{11} - b_{22}. \tag{A.41}$$

For a rigid body, there exists a frame, namely the body frame, in which the body remains at rest. Specifically, the angular momentum of the body with respect to the body frame is null. In the case of a deformable body, a frame still exists where the body's angular momentum is null: This is known as the Tisserand frame. Let $\mathrm{K} := \{\mathbf{e}_{T1}, \mathbf{e}_{T2}, \mathbf{e}_{T3}\}$ denote an orthonormal Tisserand frame for the small body. The orientation of K with respect to the inertial frame $\kappa = \{\mathbf{e}_1, \mathbf{e}_2, \mathbf{e}_3\}$ is described by $\mathbf{R} : \mathrm{K} \to \kappa$. We assume that the angular velocity of the small body, $\boldsymbol{\omega}$, is perpendicular to the orbital plane, which implies:

$$\mathbf{R}(\phi) = \begin{pmatrix} \cos\phi & -\sin\phi & 0 \\ \sin\phi & \cos\phi & 0 \\ 0 & 0 & 1 \end{pmatrix}, \tag{A.42}$$

with $\boldsymbol{\omega} = \omega\mathbf{e}_3 = \dot{\phi}\mathbf{e}_3$.

The angular momentum of the small body is denoted by $\boldsymbol{\ell}_s = \ell_s\mathbf{e}_3$, with the index s representing spin, and is given by:

$$\ell_s = \omega\,\mathrm{I}_\circ(1 - b_{33}). \tag{A.43}$$

In the context of the quadrupolar approximation, Euler's equation for the variation of ℓ_s is:

$$\dot{\ell}_s = -\frac{3G\,\mathrm{I}_\circ m_\alpha}{\|\mathbf{x}\|^5}\left\{x_1x_2(b_{22} - b_{11}) + b_{12}\left(x_1^2 - x_2^2\right)\right\}. \tag{A.44}$$

A similar equation holds for the large body.

It is imperative to note that, unlike the case of a rigid body, the deformation matrix is not constant in the Tisserand frame K.

To complete the set of Eqs. (A.40) and (A.44), we require additional equations for the deformation matrices. These equations were derived within the Lagrangian formalism and utilizing what was termed the "association principle," as detailed in Ragazzo and Ruiz (2015), Ragazzo and Ruiz (2017).

In the Tisserand frame K of the small body, the deformation matrix and the position vector are denoted by capital letters as follows:

$$\mathbf{B} = \mathbf{R}(\phi)\mathbf{b}\mathbf{R}^{-1}(\phi) \qquad \mathbf{X} = \mathbf{R}^{-1}(\phi)\mathbf{x}. \tag{A.45}$$

The equations for the deformation variables of the smaller body for the generalized Voigt model in Fig. 1 are (Ragazzo et al. 2022, Eq. (3.15))

$$\begin{aligned} &(\gamma + \alpha_0)\mathbf{B} + \Lambda = \mathbf{F} \\ &\frac{1}{\alpha}\dot{\Lambda} + \frac{1}{\eta}\Lambda = \dot{\tilde{\mathbf{B}}} \\ &\eta_j \dot{\mathbf{B}}_j + \alpha_j \mathbf{B}_j = \Lambda, \quad j = 1, \ldots, n \\ &\mathbf{B} = \tilde{\mathbf{B}} + \mathbf{B}_1 + \mathbf{B}_2 + \cdots + \mathbf{B}_n\,, \end{aligned} \tag{A.46}$$

where

- γ, with dimensions of $1/\text{time}^2$, is a parameter representing the self-gravity rigidity of the body; a larger γ indicates a stronger gravitational force holding the body together. In Fig. 1, γ would be a spring in parallel with the spring–dashpot system representing the rheology.
- $\alpha_0, \alpha, \alpha_1, \ldots$ also with dimensions of $1/\text{time}^2$, are elastic rigidity coefficients; α increases with the stiffness.
- $\eta, \eta_1, \ldots$, dimensions of $1/\text{time}$, are viscosity parameters; a body with a larger η is harder to deform at a given rate compared to a body with a smaller η.
- $\tilde{\mathbf{B}}, \mathbf{B}_1, \ldots$, are nondimensional traceless matrices that represent internal variables of the rheology;
- Λ, with dimensions $1/\text{time}^2$, is a traceless force matrix that represents the stress upon the rheology part. ($\mathbf{F} - \Lambda$ is the stress supported by self-gravity.)
- $\mathbf{F}$, with dimensions $1/\text{time}^2$, is the force matrix in the Tisserand frame K:

$$\begin{aligned} \mathbf{F} &:= \mathbf{C} + \mathbf{S} && \text{Deformation force} \\ \mathbf{C} &:= \tfrac{\omega^2}{3}\begin{pmatrix} 1 & 0 & 0 \\ 0 & 1 & 0 \\ 0 & 0 & -2 \end{pmatrix} && \text{Centrifugal force} \\ \mathbf{S} &:= \tfrac{3Gm_\alpha}{|\mathbf{X}|^5}\left(\mathbf{X}\mathbf{X}^T - \tfrac{|\mathbf{X}|^2}{3}\mathbf{1}\right) && \text{Tidal force} \end{aligned} \tag{A.47}$$

where $\mathbf{X}$ is understood as a column vector, $\mathbf{X}^T$ is the transpose of $\mathbf{X}$ (a row vector), and $\mathbf{X}\mathbf{X}^T$ is the usual product of a $n \times 1$ by $1 \times n$ matrix, which gives an $n \times n$ matrix with entries $\left(\mathbf{X}\mathbf{X}^T\right)_{ij} = X_i X_j$. The norm of a matrix is defined as $\|\mathbf{B}\|^2 = \frac{1}{2}\text{Tr}\left(\mathbf{B}^T\mathbf{B}\right)$.

Conservation of angular momentum. The orbital angular momentum is given by

$$\ell \mathbf{e}_3 = \boldsymbol{\ell} = \frac{m_\alpha m}{m_\alpha + m} \mathbf{x} \times \dot{\mathbf{x}}. \tag{A.48}$$

From Eqs. (A.40) and (A.44), we obtain

$$\dot{\boldsymbol{\ell}} = 3\frac{m_\alpha m}{|\mathbf{x}|^5} \mathbf{x} \times \left(\frac{\mathrm{I}_{\circ\alpha}}{m_\alpha} \mathbf{B}_\alpha + \frac{\mathrm{I}_\circ}{m} \mathbf{B} \right) \mathbf{x} = -\dot{\boldsymbol{\ell}}_{s\alpha} - \dot{\boldsymbol{\ell}}_s, \tag{A.49}$$

that shows the conservation of total angular momentum

$$\boldsymbol{\ell}_T := \boldsymbol{\ell} + \boldsymbol{\ell}_{s\alpha} + \boldsymbol{\ell}_s. \tag{A.50}$$

Energy. The total energy of the system is

$$E = E_{\mathrm{kcm}} + E_{\mathrm{krot}} + E_{\mathrm{def}} + E_{\mathrm{gr}} \tag{A.51}$$

where

$$E_{\mathrm{kcm}} = \frac{m_\alpha m}{m_\alpha + m} \frac{|\dot{\mathbf{x}}|^2}{2} \tag{A.52}$$

is the kinetic energy of the orbital motion;

$$E_{\mathrm{krot}} = \frac{\boldsymbol{\omega}_\alpha \cdot \mathbf{I}_\alpha \boldsymbol{\omega}_\alpha}{2} + \frac{\boldsymbol{\omega} \cdot \mathbf{I}\boldsymbol{\omega}}{2} \tag{A.53}$$

is the kinetic energy of rotation;

$$E_{\mathrm{def}} = \frac{\mathrm{I}_\circ}{2} \left((\gamma + \alpha_0) \|\mathbf{B}\|^2 + \frac{\|\Lambda\|^2}{\alpha} + \sum_{j=1}^{n} \alpha_j \|\mathbf{B}_j\|^2 \right) + \text{ Large body term} \tag{A.54}$$

is the elastic energy of deformation of the generalized Voigt model in Fig. 1; and

$$E_{\mathrm{gr}} = -\frac{G m_\alpha m}{|\mathbf{x}|} - \frac{3G}{2} \frac{1}{|\mathbf{x}|^5} \left\{ m \mathrm{I}_{\circ\alpha} (\mathbf{x} \cdot \mathbf{B}_\alpha \mathbf{x}) + m_\alpha \mathrm{I}_\circ (\mathbf{x} \cdot \mathbf{B}\mathbf{x}) \right\} \tag{A.55}$$

is the potential energy due to gravitational interactions.

Dissipation of energy. For the generalized Voigt model in Fig. 1, the dissipation function of the small body is:

$$\mathcal{D} = \frac{\mathrm{I}_\circ}{2} \left(\frac{\|\Lambda\|^2}{\eta} + \sum_{j=1}^{n} \eta_j \|\dot{\mathbf{B}}_j\|^2 \right). \tag{A.56}$$

A similar expression $\mathcal{D}_\alpha$ holds for the large body. The Lagrangian formalism with dissipation function Ragazzo and Ruiz (2015), Ragazzo and Ruiz (2017) implies that the total energy decreases along the motion:

$$\dot{E} = -(2\mathcal{D} + 2\mathcal{D}_\alpha) \leq 0. \tag{A.57}$$

Moreover, $2\mathcal{D}_\alpha$ and $2\mathcal{D}$ are the powers dissipated within the large and small bodies, respectively.

The secular Eq. (2.13) are approximations to the fundamental equations presented in this section.

B Computation of the passive deformation matrix

Passive deformation refers to the tides caused by an orbiting point mass on an extended body, while the influence of the gravitational field, resulting from the deformation on the orbit, is neglected. The equations that describe these passive deformations are obtained setting $\mathbf{B} = \mathbf{B}_\alpha = 0$ in Eqs. (A.40) and (A.44) while preserving Eq. (A.46):

$$\begin{aligned}
&\ddot{\mathbf{x}} = -G(m_\alpha + m)\frac{\mathbf{x}}{|\mathbf{x}|^3}, \quad \dot{\omega} = 0, \quad \dot{\omega}_\alpha = 0\\
&(\gamma + \alpha_0)\mathbf{B} + \Lambda = \mathbf{F}\\
&\frac{1}{\alpha}\dot{\Lambda} + \frac{1}{\eta}\Lambda = \dot{\tilde{\mathbf{B}}}\\
&\eta_j \dot{\mathbf{B}}_j + \alpha_j \mathbf{B}_j = \Lambda, \quad j = 1, \ldots, n\\
&\mathbf{B} = \tilde{\mathbf{B}} + \mathbf{B}_1 + \mathbf{B}_2 + \cdots + \mathbf{B}_n.\\
&\text{Plus deformation equations for the large body}
\end{aligned} \tag{B.58}$$

In this scenario, $\boldsymbol{\omega}$ and $\boldsymbol{\omega}_\alpha$ remain constant and $\mathbf{x}$ follows a Keplerian ellipse.

In order to write the $\mathbf{F}$ in a convenient way, we define the matrices (Ragazzo and Ruiz 2017, Eq. (41))

$$\mathbf{Y}_0 := \frac{1}{\sqrt{3}}\begin{pmatrix} 1 & 0 & 0\\ 0 & 1 & 0\\ 0 & 0 & -2\end{pmatrix}, \quad \mathbf{Y}_1 := \frac{1}{\sqrt{2}}\begin{pmatrix} 0 & 0 & 1\\ 0 & 0 & -i\\ 1 & -i & 0\end{pmatrix}, \quad \mathbf{Y}_2 := \frac{1}{\sqrt{2}}\begin{pmatrix} 1 & -i & 0\\ -i & -1 & 0\\ 0 & 0 & 0\end{pmatrix}, \tag{B.59}$$

$\mathbf{Y}_{-1} = \overline{\mathbf{Y}}_1$, and $\mathbf{Y}_{-2} = \overline{\mathbf{Y}}_2$, where the overline represents complex conjugation.

Any symmetric matrix can be written as a linear combination of the six matrices $\{\mathbf{1}, \mathbf{Y}_{-2}, \mathbf{Y}_{-1}, \mathbf{Y}_0, \mathbf{Y}_1, \mathbf{Y}_2\}$. This basis is orthonormal with respect to the Hermitean inner product $\mathbf{A} \cdot \mathbf{B} = \frac{1}{2}\mathrm{Tr}\big(\overline{\mathbf{A}}^{\mathrm{T}}\mathbf{B}\big) = \frac{1}{2}\sum_{ij}\overline{A}_{ij}B_{ij}$.

Traceless matrices that are invariant under rotation with respect to the $\mathbf{e}_3$-axis can be written as linear combinations of $\{\mathbf{Y}_{-2}, \mathbf{Y}_0, \mathbf{Y}_2\}$. These matrices have a simple transformation rule with respect to rotations about the axis $\mathbf{e}_3$, namely

$$\mathbf{R}(\theta)\mathbf{Y}_j\mathbf{R}^{-1}(\theta) = \mathrm{e}^{i\,j\,\theta}\,\mathbf{Y}_j, \quad j = -2, 0, 2. \tag{B.60}$$

An elliptic orbit in the body frame is given by

$$\begin{aligned}
\mathbf{X} &= \mathbf{R}^{-1}(\phi)\mathbf{x} = r\mathbf{R}(f + \varpi - \phi)\mathbf{e}_1\\
&= r(\cos(f + \varpi - \phi)\,\mathbf{e}_1 + \sin(f + \varpi - \phi)\,\mathbf{e}_2),
\end{aligned} \tag{B.61}$$

where f is the true anomaly and ϖ is the argument of the periapsis.

The associated tidal force matrix, Eq. (A.47), can be written as

$$\begin{aligned}
\mathbf{S} &= \frac{3Gm_\alpha}{r^3}\mathbf{R}_3(f + \varpi - \phi)\Big\{\mathbf{e}_1\mathbf{e}_1^T - \frac{1}{3}\mathbf{1}\Big\}\mathbf{R}_3^{-1}(f + \varpi - \phi)\\
&= \frac{3Gm_\alpha}{2r^3}\left\{\mathrm{e}^{-2i(f+\varpi-\phi)}\frac{\mathbf{Y}_{-2}}{\sqrt{2}} + \frac{\mathbf{Y}_0}{\sqrt{3}} + \mathrm{e}^{2i(f+\varpi-\phi)}\frac{\mathbf{Y}_2}{\sqrt{2}}\right\}.
\end{aligned} \tag{B.62}$$

In Eq. (B.62), the variables r, f, and $\phi = \omega t$ are dependent on t.

Equations (B.62) and (F.86) give a harmonic decomposition of the tidal force as follows:

$$\mathbf{S} = \frac{3Gm_\alpha}{2a^3}\sum_{l=-2}^{2}\sum_{k=-\infty}^{\infty}\mathrm{e}^{i\{t(kn-l\omega)+l\,\varpi\}}\mathbf{Y}_l U_{kl}, \tag{B.63}$$

where $U_{k,-1} = U_{k,1} = 0$ and

$$U_{k,-2} = \frac{X_k^{-3,-2}}{\sqrt{2}}, \quad U_{k0} = \frac{X_k^{-3,0}}{\sqrt{3}}, \quad U_{k2} = \frac{X_k^{-3,2}}{\sqrt{2}}. \tag{B.64}$$

The symmetry property $X_{-k}^{n,-m} = X_k^{n,m}$ implies $U_{kj} = U_{-k,-j}$.

The centrifugal force in Eq. (A.47) can be represented as

$$\mathbf{C} = \frac{\omega^2}{\sqrt{3}}\mathbf{Y}_0. \tag{B.65}$$

To obtain the almost periodic solution[8] of the deformation equation solving for each Fourier mode separately suffices.

To simplify the notation, we consider a simple harmonic force term of the form

$$\mathbf{F}(t) = \mathbf{F}' \mathrm{e}^{i\,\sigma\,t}$$

where $\mathbf{F}'$ is a complex amplitude matrix and $\sigma \in \mathbb{R}$ is the constant forcing frequency.

If we do the substitutions

$$\mathbf{B} \to \mathbf{B}'\,\mathrm{e}^{i\,\sigma\,t}, \quad \mathbf{B}_j \to \mathbf{B}'_j\,\mathrm{e}^{i\,\sigma\,t}, \quad \Lambda \to \Lambda'\,\mathrm{e}^{i\,\sigma\,t},$$

where $\mathbf{B}', \mathbf{B}'_j$ and $\Lambda_\mathbf{j}{}'$ are understood as constant complex amplitude matrices, into Eq. (A.46), then we obtain after some simplifications

$$\left\{\gamma + \alpha_0 + \left(\frac{1}{\alpha} + \frac{1}{\eta i\sigma} + \sum_{j=1}^{n} \frac{1}{\alpha_j + i\sigma\eta_j}\right)^{-1}\right\} \mathbf{B}' = \mathbf{F}'. \tag{B.66}$$

The term $\frac{1}{\alpha} + \frac{1}{\eta i\sigma} + \sum_{j=1}^{n} \frac{1}{\alpha_j + i\sigma\eta_j}$ is the complex rigidity $J(\sigma)$ of the generalized Voigt model when $\alpha_0 = 0$ (Ragazzo et al. 2022, equation 4.23).

The complex Love number at frequency σ can be written as (Correia et al. 2018, Section 4):

$$k_2(\sigma) = \frac{3\,\mathrm{I}_\circ G}{R^5} \frac{1}{\gamma + \alpha_0 + J^{-1}(\sigma)}. \tag{B.67}$$

Note: $k_2(-\sigma) = \overline{k}_2(\sigma)$. Therefore, Eq. (B.66) can be written as

$$\mathbf{B}' = \frac{R^5}{3\,\mathrm{I}_\circ G} k_2(\sigma)\mathbf{F}'. \tag{B.68}$$

Applying Eq. (B.68) to each Fourier coefficient of $\mathbf{F} = \mathbf{S} + \mathbf{C}$, where $\mathbf{S}$ and $\mathbf{C}$ are defined in Eqs. (B.63) and (B.65), respectively, we obtain the passive deformation matrix

$$\mathbf{B}(t) = k_\circ \zeta_c \frac{\mathbf{Y}_0}{3\sqrt{3}} + \zeta_T \sum_{l=-2}^{2} \sum_{k=-\infty}^{\infty} \mathrm{e}^{i\{t(kn-l\omega)+l\,\varpi\}} k_2(kn - l\omega)\mathbf{Y}_l U_{kl}, \tag{B.69}$$

where $k_\circ = k_2(0)$ is the secular Love number and

$$\zeta_c := \frac{R^5\omega^2}{G\,\mathrm{I}_\circ} \quad \text{and} \quad \zeta_T := \frac{m_\alpha R^5}{2\,\mathrm{I}_\circ a^3}. \tag{B.70}$$

[8] A function is almost periodic if and only if it can be uniformly approximated by trigonometric polynomials.

C The average angular velocity of the principal axes of inertia

The passive deformation matrix in Eq. (B.69) can be written as

$$\begin{aligned}
&\mathbf{B}(t) = b_0(t)\mathbf{Y}_0 + b_{-2}(t)\mathbf{Y}_{-2} + b_2(t)\mathbf{Y}_2 \quad \text{where} \\
&b_0(t) := \frac{k_\circ \zeta_c}{3\sqrt{3}} + \frac{\zeta_T}{\sqrt{3}} \sum_{k=-\infty}^{\infty} \mathrm{e}^{itkn} X_k^{-3,0}(e) k_2(kn) \\
&b_2(t) := \frac{\zeta_T}{\sqrt{2}} \mathrm{e}^{i2(-\omega t + \varpi)} \sum_{k=-\infty}^{\infty} \mathrm{e}^{itkn} X_k^{-3,2}(e) k_2(kn - 2\omega),
\end{aligned} \tag{C.71}$$

with $b_{-2}(t) = \overline{b}_2(t)$.

Let $I_1(t) \le I_2(t) \le I_3(t)$ be the principal moments of inertia of the body at time t and $B_1(t) \ge B_2(t) \ge B_3(t)$ be the corresponding elements of the deformation matrix. The frame of principal axes of inertia $\mathrm{K}_p := \{\mathbf{e}_{p1}, \mathbf{e}_{p2}, \mathbf{e}_{p3}\}$ is defined by three vectors in the direction of the axes associated with $B_1(t)$, $B_2(t)$, $B_3(t)$, respectively, such that K_p and the Tisserand frame K have the same orientation.

The diagonalization of the matrix $\mathbf{B}(t)$ is done by means of a rotation matrix $\mathbf{R}(\theta)$ about the axis $\mathbf{e}_3$. The transformation $\mathbf{R}(\theta) : \mathrm{K} \to \mathrm{K}_p$ maps the Tisserand frame to the principal axes frame. Equations (C.71) and (B.60) and the definition of $\mathbf{Y}_2 = \overline{\mathbf{Y}}_{-2}$ in Eq. (B.59) imply that either $\theta = -\frac{1}{2}\arg(b_2)$ or $\theta = -\frac{1}{2}\arg(b_2) + \pi$. We will use $\theta = -\frac{1}{2}\arg(b_2)$. The definition of $b_2(t)$ in Eq. (C.71) implies

$$\theta(t) = -\frac{1}{2}\arg(b_2) = \omega t - \varpi - \frac{1}{2}\arg\Big(\sum_{k=-\infty}^{\infty} \mathrm{e}^{itkn} X_k^{-3,2}(e) k_2(kn - 2\omega) \Big). \tag{C.72}$$

After diagonalization the matrix $\mathbf{B}$ becomes

$$\mathbf{R}(\theta)\mathbf{B}\mathbf{R}^{-1}(\theta) = b_0\mathbf{Y}_0 + |b_2|\big(\mathbf{Y}_{-2} + \mathbf{Y}_2\big) = \frac{1}{\sqrt{3}} \begin{pmatrix} b_0 & 0 & 0 \\ 0 & b_0 & 0 \\ 0 & 0 & -2b_0 \end{pmatrix} + \sqrt{2} \begin{pmatrix} |b_2| & 0 & 0 \\ 0 & -|b_2| & 0 \\ 0 & 0 & 0 \end{pmatrix}. \tag{C.73}$$

The orientation of the Tisserand frame K with respect to the inertial frame κ is given by $\mathbf{R}(\phi) : \mathrm{K} \to \kappa$, Eq. (A.42). So, the orientation of the principal axes frame with respect to the inertial frame is given by $\mathbf{R}(\phi)\mathbf{R}^{-1}(\theta) = \mathbf{R}(\phi - \theta) : \mathrm{K}_p \to \kappa$ or $\mathbf{R}(\psi) : \mathrm{K}_p \to \kappa$ where $\psi = \phi - \theta$. Therefore, for fixed values of spin $\omega = \dot{\phi}$ and mean motion n, we define the average angular velocity of the principal axes of inertia as:

$$\omega_p := \lim_{t\to\infty} \frac{\psi(t)}{t} = \lim_{t\to\infty} \frac{\phi(t) - \theta(t)}{t} = \lim_{t\to\infty} \frac{\omega t - \theta(t)}{t}. \tag{C.74}$$

Using Eq. (C.72) we obtain

$$\omega_p = \frac{1}{2} \lim_{t\to\infty} \frac{1}{t} \arg\Big(\underbrace{\sum_{k=-\infty}^{\infty} \mathrm{e}^{itkn} X_k^{-3,2}(e) k_2(kn - 2\omega)}_{=P(t)} \Big). \tag{C.75}$$

The function $P(t)$ within parentheses in Eq. (C.75) is periodic with period $T = \frac{2\pi}{n}$. Therefore, $\arg\big(P(t+T)\big) = 2\pi\, j + \arg\big(P(t)\big)$ where j is an integer. This implies

$$\omega_p = \frac{1}{2} \lim_{l\to\infty} \frac{1}{lT} \arg\big(P(lT)\big) = \frac{1}{2} \lim_{l\to\infty} \frac{2\pi\, jl + \arg\big(P(0)\big)}{lT} = \frac{j}{2} n. \tag{C.76}$$

Since the map $t \to \arg\big(P(t)\big)$ is periodic with period T, this function can be understood as the lift of a function from the circle $\mathbb{R}/(T\mathbb{Z})$ to the circle $\mathbb{R}/(2\pi\mathbb{Z})$. In this context, the integer j is the degree of the map from $\mathbb{R}/(T\mathbb{Z})$ to $\mathbb{R}/(2\pi\mathbb{Z})$.[9] The degree is invariant under continuous deformation of the function $t \to \arg\big(P(t)\big)$. Since P depends differentiably on (ω, e, n) and also on all parameters of the rheology within the usual range of variation of these variables, we conclude that j is constant. For $e = 0$, the only nonzero Hansen coefficient is $X_2^{-3,2}(0) = 1$. In this case:

$$\arg\big(P(t)\big) = \arg\big(e^{it2n}k_2(2n-2\omega)\big) = t\cdot 2\cdot\frac{2\pi}{T} + \text{const} \Rightarrow j = 2. \tag{C.77}$$

So, as expected:

$$\omega_p = n \tag{C.78}$$

independently of (ω, e, n) and the rheology.

D The average dissipation of energy and average torque

The energy dissipated in the smaller body is $-2\mathcal{D}$, where $\mathcal{D}$ is the dissipation function as given in Eq. (A.56). The average dissipation function over the orbital motion is approximately given by

$$\langle\mathcal{D}\rangle := \lim_{t\to\infty}\int_0^T \mathcal{D}\mathrm{d}t = \frac{\mathrm{I}_\circ}{2}\lim_{t\to\infty}\int_0^T\left(\frac{\|\Lambda\|^2}{\eta} + \sum_{j=1}^{n}\eta_j\|\dot{\mathbf{B}}_j\|^2\right)\mathrm{d}t, \tag{D.79}$$

where $(\mathbf{B}, \Lambda, \ldots)$ are the components of the solution to Eq. (A.46) under the passive deformation hypothesis.

From Eq. (A.46), we obtain:

$$\begin{aligned}
&(\gamma+\alpha_0)\cancel{\langle\dot{\mathbf{B}}\cdot\mathbf{B}\rangle} + \langle\dot{\mathbf{B}}\cdot\Lambda\rangle = \cancel{\langle\dot{\mathbf{B}}\cdot\mathbf{C}\rangle} + \langle\dot{\mathbf{B}}\cdot\mathbf{S}\rangle\\
&\cancel{\frac{1}{\alpha}\langle\Lambda\cdot\dot{\Lambda}\rangle} + \frac{1}{\eta}\|\Lambda\|^2 = \langle\Lambda\cdot\dot{\tilde{\mathbf{B}}}\rangle\\
&\eta_j\|\dot{\mathbf{B}}_j\|^2 + \alpha_j\cancel{\langle\dot{\mathbf{B}}_j\cdot\mathbf{B}_j\rangle} = \langle\dot{\mathbf{B}}_j\cdot\Lambda\rangle, \quad j = 1,\ldots,n\\
&\langle\dot{\mathbf{B}}\cdot\Lambda\rangle = \langle\dot{\tilde{\mathbf{B}}}\cdot\Lambda\rangle + \langle\dot{\mathbf{B}}_1\cdot\Lambda\rangle + \langle\dot{\mathbf{B}}_2\cdot\Lambda\rangle + \cdots + \langle\dot{\mathbf{B}}_n\cdot\Lambda\rangle,
\end{aligned} \tag{D.80}$$

where we used that the centrifugal force $\mathbf{C}$, Eq. (B.65), is constant. These equations imply

$$\langle\mathcal{D}\rangle = \frac{\mathrm{I}_\circ}{2}\langle\dot{\mathbf{B}}\cdot\mathbf{S}\rangle, \tag{D.81}$$

where $\mathbf{S}$ and $\mathbf{B}$ are given in Eqs. (B.63) and (B.69), respectively.

In the computation of the averaging $\langle\dot{\mathbf{B}}\cdot\mathbf{S}\rangle$, the following identities are useful: $\mathbf{Y}_l\cdot\mathbf{Y}_{-m} = \delta_{lm}$, $U_{kl} = U_{-k,-l}$, and $k_2(-\sigma) = \bar{k}_2(\sigma)$. After some computations, we obtain Eq. (2.10).

The total energy, as given in Eq. (A.51), includes terms that depend on the deformation matrices. If we set $\mathbf{B} = \mathbf{B}_\alpha = 0$ in this equation and assume that the orbit is Keplerian and the spins are constant, then we obtain the energy function $E_\circ$, as presented in Eq. (2.6), for

[9] The number of times the domain circle $\mathbb{R}/(T\mathbb{Z})$ wraps around the range circle $\mathbb{R}/(2\pi\mathbb{Z})$ under the mapping.

a system of two rigid spherical bodies. It is a natural assumption that the energy dissipated in the two bodies is subtracted from $E_\circ$. This assumption leads to Eq. (2.11).

The average torque is computed as the average of the right-hand side of Eq. (A.44),

$$\langle \mathrm{T} \rangle := \lim_{t\to\infty} \int_0^T -\frac{3G\,\mathrm{I}_\circ m_\alpha}{\|\mathbf{x}\|^5}\left\{x_1x_2(b_{22}-b_{11}) + b_{12}\left(x_1^2 - x_2^2\right)\right\}\mathrm{d}t, \tag{D.82}$$

where $\mathbf{B}$ represents the passive deformation matrix and $\mathbf{x}$ determines Keplerian ellipses. Standard computations lead to Eq. (2.12).

Equations (2.11) and (2.12) imply Eq. (2.13).

E The functions $k_\infty(\tau_1, \tau_2)$ and $h_1(\tau_1, \tau_2)$.

We define τ_1 and τ_2 such that $\tau_1 < \tau_2$. Equation (2.34) can be solved for k_∞ and h_1 as follows:

$$\begin{aligned} k_\infty &= k_\infty(\tau_1,\tau_2) = k_R + \frac{k_I}{n_{\mathrm{mer}}}\left(\frac{1}{\tau_1} + \frac{1}{\tau_2} - \frac{n_{\mathrm{mer}}\tau_c}{\tau_1+\tau_2}\right), \\ h_1 &= h_1(\tau_1,\tau_2) = \frac{(n_{\mathrm{mer}}^2\tau_1^2+1)\tau_2(\tau_2-\tau_c)}{(\tau_2-\tau_1)(\tau_1+\tau_2+\tau_c(n_{\mathrm{mer}}^2\tau_1\tau_2-1))}, \end{aligned} \tag{E.83}$$

where $n_{\mathrm{mer}}\tau_c := \frac{k_\circ - k_R}{-k_I}$.

The inequality $h_1(\tau_1,\tau_2) > 0$ is equivalent to

$$\tau_1\frac{(n_{\mathrm{mer}}^2\tau_c\tau_2+1)}{\tau_2-\tau_c} + 1 > 0. \tag{E.84}$$

We conclude that (E.84) is satisfied for $\tau_2 > \tau_c$. The inequality $h_1(\tau_1,\tau_2) < 1$ is equivalent to

$$\frac{\tau_1\left(n_{\mathrm{mer}}^2\tau_2^2+1\right)(\tau_c-\tau_1)}{\tau_2-\tau_c} > 0. \tag{E.85}$$

We conclude that the inequalities $0 < h_1 < 1$ hold for $\tau_2 > \tau_1$ if and only if $\tau_1 < \tau_c < \tau_2$. For τ_2 fixed, $\lim_{\tau_1\to\tau_c} h_1(\tau_1,\tau_2) = 1$, and for τ_1 fixed, $\lim_{\tau_2\to\tau_c} h_1(\tau_1,\tau_2) = 0$.

F An identity for Hansen coefficients and the accuracy of eccentricity expansions

If a is the semi-major axis, e is the eccentricity, f is the true anomaly, and M is the mean anomaly, then the Hansen coefficients are defined by

$$\left(\frac{r}{a}\right)^n e^{imf} = \sum_{k=-\infty}^{\infty} X_k^{n,m}(e)e^{ikM}, \tag{F.86}$$

where n, m, k are integers. This definition is equivalent to

$$X_k^{n,m}(e) = \frac{1}{2\pi}\int_0^{2\pi}\left(\frac{r}{a}\right)^n \cos(mf - kM)\,\mathrm{d}M, \tag{F.87}$$

which implies $X_k^{n,-m} = X_{-k}^{n,m}$.

The expression for the averaged torque (2.12) is the sum of several terms proportional to $\left(X_k^{-3,2}(e)\right)^2$. The function $X_k^{-3,2}(e)$ can be expanded into an infinite power series in e. For a given integer $N > 1$, let $\tilde{X}_k^{-3,2}$ denote the truncation of this series at order e^N. It can be shown that $X_k^{n,m} = \mathcal{O}(e^{|m-k|})$, which implies $X_k^{-3,2} = \mathcal{O}(e^{|2-k|})$. Therefore, expansions in eccentricity up to order N mean that $\tilde{X}_k^{-3,2} = 0$ if k does not satisfy $2 - N \le k \le 2 + N$.

Question: How large can $0 < e < 1$ be for an accurate estimate of the average torque if we substitute $X_k^{-3,2}$ with $\tilde{X}_k^{-3,2}$ in Eq. (2.12)?

Neglecting the constant factor in the definition of the average torque, the difference to be estimated to answer this question is:

$$\sum_{k=-\infty}^{\infty} \left\{ \left(X_k^{-3,2}(e)\right)^2 \operatorname{Im} k_2(k\dot{M} - 2\omega) - \sum_{k=2-N}^{2+N} \left(\tilde{X}_k^{-3,2}(e)\right)^2 \operatorname{Im} k_2(k\dot{M} - 2\omega) \right\}.$$

If e, $\dot{M}$, and ω are assumed to be independent in the above sum (which is not the case in this paper), then for $\dot{M} = 0$, the factor $k_2(-2\omega)$ can be taken out of the sum, and it is enough to estimate:

$$\sum_{k=-\infty}^{\infty} \left(X_k^{-3,2}(e)\right)^2 - \sum_{k=2-N}^{2+N} \left(\tilde{X}_k^{-3,2}(e)\right)^2.$$

Applying Parseval's identity to the first term in this sum, we get:

$$\sum_{k=-\infty}^{\infty} \left(X_k^{-3,2}(e)\right)^2 = \frac{1}{2\pi} \int_0^{2\pi} \frac{e^{i2f}}{r^3} \frac{e^{-i2f}}{r^3} \, \mathrm{d}M = \frac{1}{2\pi} \int_0^{2\pi} \frac{1}{r^6} \, \mathrm{d}M = X_0^{-6,0}. \quad \text{(F.88)}$$

From Laskar and Boué (2010), $X_0^{-6,0} = \frac{\frac{3e^4}{8} + 3e^2 + 1}{(1-e^2)^{9/2}}$. So, in the case $\dot{M} = 0$, we conclude that the substitution $X_k^{-3,2} \to \tilde{X}_k^{-3,2}$ is good if and only if

$$\Delta(e) := \left| \underbrace{\frac{\frac{3e^4}{8} + 3e^2 + 1}{\left(1 - e^2\right)^{9/2}}}_{= X_0^{-6,0}(e)} - \underbrace{\sum_{k=2-N}^{2+N} \left(\tilde{X}_k^{-3,2}(e)\right)^2}_{App(e)} \right| \text{ is small.} \quad \text{(F.89)}$$

This criterion holds only for $\dot{M} = 0$, but we can loosely expect it to be a necessary condition for the validity of the approximation even when $\dot{M} \neq 0$.

In Fig. 10, we show how to check the approximation for $N = 20$.

We finally remark that in Eq. (2.10), in addition to the sum with terms proportional to $\left(X_k^{-3,2}\right)^2$, there is a sum with terms proportional to $\left(X_k^{-3,0}\right)^2$. Using Parseval's identity, we obtain:

$$\sum_{k=-\infty}^{\infty} \left(X_k^{-3,0}(e)\right)^2 = \frac{1}{2\pi} \int_0^{2\pi} \frac{1}{r^3} \frac{1}{r^3} \, \mathrm{d}M = \frac{1}{2\pi} \int_0^{2\pi} \frac{1}{r^6} \, \mathrm{d}M = X_0^{-6,0}. \quad \text{(F.90)}$$

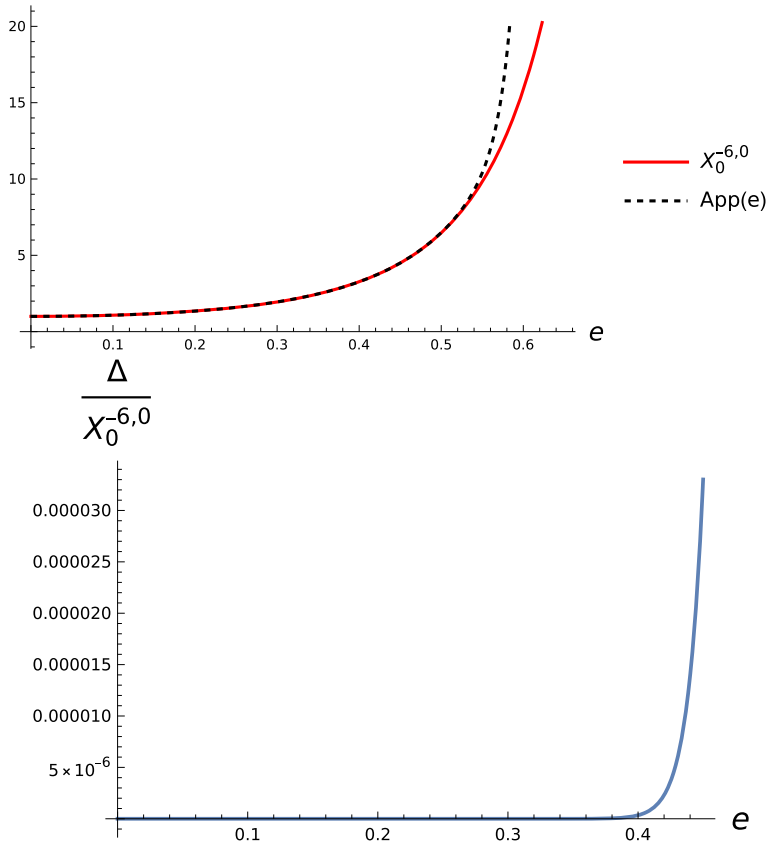

Fig. 10 For the truncation of $X_k^{-3,2}(e)$ to order e^{20} ($N = 20$), and using the notation in Eq. (F.89), we present the plots of $X_0^{-6,0}(e)$ and $App(e)$ (ABOVE panel) and $\Delta(e)/X_0^{-6,0}(e)$ (BELOW panel). The ABOVE panel shows that the approximation is satisfactory up to $e = 0.5$ ($\Delta(e)/X_0^{-6,0}(e) \approx 2 \times 10^{-3}$). The BELOW panel indicates that the approximation is very good up to $e = 0.4$ ($\Delta(e)/X_0^{-6,0}(e) \approx 4 \times 10^{-7}$)

Therefore, we can combine the criterion in Eq. (F.89) with

$$\left| \frac{\frac{3e^4}{8} + 3e^2 + 1}{\left(1 - e^2\right)^{9/2}} - \sum_{k=-N}^{N} \left(\tilde{X}_k^{-3,0}(e) \right)^2 \right| \text{ is small.} \tag{F.91}$$

This allows us to estimate the accuracy of the partial sums in Eq. (2.10) after truncation in eccentricity. Computations similar to those in Fig. 10 show that truncating $\left(X_k^{-3,0}\right)^2$ in eccentricity is less problematic than truncating $\left(X_k^{-3,2}\right)^2$.

Acknowledgements We would like to thank Michael Efroimsky and an anonymous referee for their valuable suggestions and improvements to the original version of this paper. C. R. is partially supported by FAPESP grants 2016/25053-8 and 2023/07076-4. L. R. S. is supported in part by FAPEMIG under Grants No. RED-00133-21 and APQ-02153-23.

Declarations

Conflict of interest On behalf of all authors, the corresponding author states that there is no conflict of interest.

References

Alexander, M.: The weak friction approximation and tidal evolution in close binary systems. Astrophys. Space Sci. **23**, 459–510 (1973)

Baland, R.-M., Yseboodt, M., Rivoldini, A., Van Hoolst, T.: Obliquity of Mercury: influence of the precession of the pericenter and of tides. Icarus **291**, 136–159 (2017)

Bland, D.: Linear Viscoelasticity. Pergamon Press, Oxford (1960)

Boué, G., Correia, A.C., Laskar, J.: Complete spin and orbital evolution of close-in bodies using a Maxwell viscoelastic rheology. Celest. Mech. Dyn. Astron. **126**(1–3), 31–60 (2016)

Boué, G., Efroimsky, M.: Tidal evolution of the Keplerian elements. Celest. Mech. Dyn. Astron. **131**, 1–46 (2019)

Breuer, D., Hauck, S.A., Buske, M., Pauer, M., Spohn, T.: Interior evolution of mercury. Space Sci. Rev. **132**, 229–260 (2007)

Consorzi, A., Melini, D., Spada, G.: Relation between the moment of inertia and the k_2 Love number of fluid extra-solar planets. Astron. Astrophys. **676**, A21 (2023)

Correia, A., Ragazzo, C., Ruiz, L.: The effects of deformation inertia (kinetic energy) in the orbital and spin evolution of close-in bodies. Celest. Mech. Dyn. Astron. **130**(8), 51 (2018)

Correia, A.C., Boué, G., Laskar, J., Rodríguez, A.: Deformation and tidal evolution of close-in planets and satellites using a Maxwell viscoelastic rheology. Astron. Astrophys. **571**, A50 (2014)

Correia, A.C., Valente, E.F.: Tidal evolution for any rheological model using a vectorial approach expressed in Hansen coefficients. Celest. Mech. Dyn. Astron. **134**(3), 24 (2022)

Efroimsky, M.: Bodily tides near spin–orbit resonances. Celest. Mech. Dyn. Astron. **112**(3), 283–330 (2012)

Ferraz-Mello, S.: Tidal synchronization of close-in satellites and exoplanets. A rheophysical approach. Celest. Mech. Dyn. Astron. **116**(2), 109–140 (2013)

Ferraz-Mello, S.: Tidal synchronization of close-in satellites and exoplanets: II. Spin dynamics and extension to mercury and exoplanet host stars. Celest. Mech. Dyn. Astron. **122**, 359–389 (2015)

Ferraz-Mello, S.: Planetary tides: theories. Satell. Dyn. Space Miss. (2019). https://doi.org/10.1007/978-3-030-20633-8_1

Ferraz-Mello, S.: On tides and exoplanets. Proc. Int. Astron. Union **15**(S364), 20–30 (2021)

Ferraz-Mello, S., Beaugé, C., Folonier, H.A., Gomes, G.O.: Tidal friction in satellites and planets. The new version of the creep tide theory. Eur. Phys. J. Spec. Top. **229**, 1441–1462 (2020)

Fienga, A., Deram, P., Viswanathan, V., Ruscio, A., Bernus, L., Durante, D., Gastineau, M., Laskar, J.: *INPOP19a Planetary Ephemerides*. PhD thesis, IMCCE (2019)

Folonier, H., Ferraz-Mello, S., Andrade-Ines, E.: Tidal synchronization of close-in satellites and exoplanets. III. Tidal dissipation revisited and application to Enceladus. Celest. Mech. Dyn. Astron. **130**(12), 78 (2018)

Genova, A., Goossens, S., Mazarico, E., Lemoine, F.G., Neumann, G.A., Kuang, W., Sabaka, T.J., Hauck, S.A., Smith, D.E., Solomon, S.C., et al.: Geodetic evidence that Mercury has a solid inner core. Geophys. Res. Lett. **46**(7), 3625–3633 (2019)

Gevorgyan, Y.: Homogeneous model for the TRAPPIST-1e planet with an icy layer. Astron. Astrophys. **650**, A141 (2021)

Gevorgyan, Y., Boué, G., Ragazzo, C., Ruiz, L.S., Correia, A.C.: Andrade rheology in time-domain. Application to Enceladus' dissipation of energy due to forced libration. Icarus **343**, 113610 (2020)

Gevorgyan, Y., Matsuyama, I., Ragazzo, C.: Equivalence between simple multilayered and homogeneous laboratory-based rheological models in planetary science. Mon. Not. R. Astron. Soc. **523**(2), 1822–1831 (2023)

Goldreich, P.: Final spin states of planets and satellites. Astron. J. **71**, 1 (1966)

Goldreich, P., Peale, S.: Spin–orbit coupling in the solar system. Astron. J. **71**, 425 (1966)

Gomes, G.O., Folonier, H.A., Ferraz-Mello, S.: Rotation and figure evolution in the creep tide theory: a new approach and application to Mercury. Celest. Mech. Dyn. Astron. **131**(12), 56 (2019)

Goossens, S., Renaud, J.P., Henning, W.G., Mazarico, E., Bertone, S., Genova, A.: Evaluation of recent measurements of Mercury's moments of inertia and tides using a comprehensive Markov Chain Monte Carlo method. Planet. Sci. J. **3**(2), 37 (2022)

Hut, P.: Tidal evolution in close binary systems. Astron. Astrophys. **99**, 126–140 (1981)

Kaula, W.M.: Tidal dissipation by solid friction and the resulting orbital evolution. Rev. Geophys. **2**(4), 661–685 (1964)
Laskar, J., Boué, G.: Explicit expansion of the three-body disturbing function for arbitrary eccentricities and inclinations. Astron. Astrophys. **522**, A60 (2010)
Makarov, V.V.: Conditions of passage and entrapment of terrestrial planets in spin–orbit resonances. Astrophys. J. **752**(1), 73 (2012)
Makarov, V.V., Berghea, C., Efroimsky, M.: Dynamical evolution and spin–orbit resonances of potentially habitable exoplanets: the case of gj 581d. Astrophy. J. **761**(2), 83 (2012)
Makarov, V.V., Efroimsky, M.: No pseudosynchronous rotation for terrestrial planets and moons. Astrophys. J. **764**(1), 27 (2013)
Matsuyama, I., Nimmo, F.: Gravity and tectonic patterns of Mercury: effect of tidal deformation, spin–orbit resonance, nonzero eccentricity, despinning, and reorientation. J. Geophys. Res.: Planet. (2009). https://doi.org/10.1029/2008JE003252
Mignard, F.: The evolution of the lunar orbit revisited. I. Moon Planet **20**(3), 301–315 (1979)
Noyelles, B., Frouard, J., Makarov, V.V., Efroimsky, M.: Spin–orbit evolution of Mercury revisited. Icarus **241**, 26–44 (2014)
Ogilvie, G.I.: Tidal dissipation in stars and giant planets. Ann. Rev. Astron. Astrophys. **52**, 171–210 (2014)
Ragazzo, C.: The theory of figures of Clairaut with focus on the gravitational modulus: inequalities and an improvement in the Darwin-Radau equation. São Paulo J. Math. Sci. **14**, 1–48 (2020)
Ragazzo, C., Boué, G., Gevorgyan, Y., Ruiz, L.S.: Librations of a body composed of a deformable mantle and a fluid core. Celest. Mech. Dyn. Astron. **134**(2), 10 (2022)
Ragazzo, C., dos Santos, L.R.: Spin–orbit synchronization and singular perturbation theory. São Paulo J. Math. Sci. (2024). https://doi.org/10.1007/s40863-024-00418-7
Ragazzo, C., Ruiz, L.: Dynamics of an isolated, viscoelastic, self-gravitating body. Celest. Mech. Dyn. Astron. **122**(4), 303–332 (2015)
Ragazzo, C., Ruiz, L.: Viscoelastic tides: models for use in Celestial Mechanics. Celest. Mech. Dyn. Astron. **128**(1), 19–59 (2017)
Rochester, M., Smylie, D.: On changes in the trace of the Earth's inertia tensor. J. Geophys. Res. **79**(32), 4948–4951 (1974)
Sabadini, R., Vermeersen, B., Cambiotti, G.: Global Dynamics of the Earth. Springer (2016)
Singer, S.: The origin of the Moon and geophysical consequences. Geophys. J. Int. **15**(1–2), 205–226 (1968)
Steinbrügge, G., Padovan, S., Hussmann, H., Steinke, T., Stark, A., Oberst, J.: Viscoelastic tides of Mercury and the determination of its inner core size. J. Geophys. Res.: Planet. **123**(10), 2760–2772 (2018)